PHYSICAL REVIEW D **83,** 043007 (2011)

Stability of general-relativistic accretion disks

Oleg Korobkin,[1,2] Ernazar B. Abdikamalov,[2] Erik Schnetter,[2,1] Nikolaos Stergioulas,[3] and Burkhard Zink[4]
[1]*Department of Physics and Astronomy, Louisiana State University, Baton Rouge, Louisiana 70803, USA*
[2]*Center for Computation and Technology, Louisiana State University, Baton Rouge, Louisiana 70803, USA*
[3]*Department of Physics, Aristotle University of Thessaloniki, Thessaloniki, 54124 Greece*
[4]*Theoretical Astrophysics, University of Tübingen, Tübingen 72076, Germany*
(Received 12 November 2010; published 18 February 2011)

Self-gravitating relativistic disks around black holes can form as transient structures in a number of astrophysical scenarios such as binary neutron star and black hole-neutron star coalescences, as well as the core collapse of massive stars. We explore the stability of such disks against runaway and nonaxisymmetric instabilities using three-dimensional hydrodynamics simulations in full general relativity using the THOR code. We model the disk matter using the ideal fluid approximation with a Γ-law equation of state with $\Gamma = 4/3$. We explore three disk models around nonrotating black holes with disk-to-black hole mass ratios of 0.24, 0.17, and 0.11. Because of metric blending in our initial data, all of our initial models contain an initial axisymmetric perturbation which induces radial disk oscillations. Despite these oscillations, our models do not develop the runaway instability during the first several orbital periods. Instead, all of the models develop unstable nonaxisymmetric modes on a dynamical time scale. We observe two distinct types of instabilities: the Papaloizou-Pringle and the so-called intermediate type instabilities. The development of the nonaxisymmetric mode with azimuthal number $m = 1$ is accompanied by an outspiraling motion of the black hole, which significantly amplifies the growth rate of the $m = 1$ mode in some cases. Overall, our simulations show that the properties of the unstable nonaxisymmetric modes in our disk models are qualitatively similar to those in the Newtonian theory.

DOI: 10.1103/PhysRevD.83.043007 PACS numbers: 98.70.Rz, 04.25.dg, 04.30.Db

I. INTRODUCTION

Thick relativistic accretion disks and tori around black holes (BHs) can form as transient structures in several astrophysical scenarios, including core collapse of massive stars [1–12] and the merger of neutron star (NS) [13–27] and NS-BH binaries [19,28–37]. Many models of gamma-ray bursts (GRBs) rely on the existence of massive dense accretion disks around BHs [1,3,38–40]. The observed $\sim 10^{51}$ erg energy powering GRBs [39,41,42] is believed to be coming from either the accretion disk and/or rotation of the central object. If this energy comes from the disk,[1] then—assuming that the efficiency of converting disk energy into that of a GRB can at most be $\sim 10\%$ as in many other astrophysical scenarios [46]—the accretion disk should have a mass of $\gtrsim 0.01\mathcal{M}_\odot$. Recent numerical simulations have demonstrated that the mass of the disk resulting from binary NS-NS (BH-NS) mergers, which are thought to be candidates for the central engine of short GRBs (see, e.g., [40,47], but also [48]), can be in the range of ~ 0.01–$0.2\mathcal{M}_\odot$ [13,19,20,33]. Because of their larger initial mass, in core collapse of massive stars, which are believed to be progenitors of long GRBs[2] [1,2,6], significantly more mass is available for forming disks [3,50].

The neutrino-annihilation mechanism for triggering GRBs [40,51,52], in which neutrinos emitted by the disk annihilate predominantly at the rotation axis to produce $e^+ - e^-$ pairs and deposit energy behind the jet, rely on super-Eddington accretion rates, which can take place only in high-density ($\rho \sim 10^{12}\ \mathrm{g\,cm^{-3}}$) disks. Moreover, the efficiency of neutrino annihilation at the rotation axis and the requirement of a small baryon load of the relativistic ejecta [39,41,53] was shown to strongly favor a toroidal structure for accreting matter [54,55].

The duration of prompt γ-ray emission is >2 s ($\lesssim 2$ s) for long (short) GRBs, while that of the later-time non-γ-ray emission can be as long as $\sim 10^5$ s (e.g., [42]). Recent observations of GRB afterglows have revealed a variety of late-time emission processes, including x-ray plateaus, flares, and chromatic breaks [42], some of which can persist up to $\sim 10^5$ s following the initial GRB prompt emission (see, e.g., [42] for a recent review). The amount of energy released in the late-time emission phase can be comparable to or even larger than that produced during the

---

[1] In alternative models, the GRB is powered by the rotation energy of the central object. If the latter is a BH, then the rotation can be converted through the Blandford-Znajek mechanism [43]. If the central object is a NS, then its energy can be transformed through magnetic fields [44,45].

[2] Note that although all of the long GRBs are believed to be produced by core collapse of massive stars, not all of the latter can produce long GRBs: In order to produce a GRB, a precollapse star is probably required to be rapidly rotating [1,12,49].

prompt emission phase. Both the prompt and the late-time emissions can be explained as the result of the activity of the central engine (see, e.g., [42,56]), although alternatives models exist (see, e.g., [57–59]). If the emission energy comes from the disk, such long durations of observed GRB emission either require the disks to accrete in a quasistable manner for a sufficiently long period of time or require the engine to be restarted in some way.

Early studies of the stability of accretion disks have revealed that they can be subject to several types of axisymmetric and/or nonaxisymmetric instabilities in a number of circumstances [60–66]. Instabilities can lead to highly variable and unstable accretion rates, posing a serious challenge to the viability of "accretion-powered" GRB models. The so-called dynamical runaway instability of thick accretion disks around BHs was first discovered by Abramowicz, Calvani, and Nobili [60]. This instability is similar to the dynamical instability in close binary systems, when the more massive companion overflows its Roche lobe. In such a case, the radius of the Roche lobe shrinks faster than the radius of the companion, leading to a catastrophic disruption of the latter. In disk + BH systems, a toroidal surface analogous to the Roche lobe can be found. A meridional cut of this surface has a cusp located at the L_1 Lagrange point. If the disk is overflowing this toroidal "Roche lobe", then the mass transfer through the cusp will advance the cusp outwards inside the disk. This can result in a catastrophic growth of the mass transfer and disruption of the disk in just a few dynamical time scales.

Abramowicz, Calvani, and Nobili [60] studied the properties of mass transfer using many simplifying assumptions: a pseudo-Newtonian potential for BH gravity [67], constant specific angular momentum of the disk, and approximate treatment of the disk self-gravity. They found that the runaway instability occurs for a large range of parameters, such as the disk radius and the disk-to-BH mass ratio M_D/M_{BH}. Subsequent and somewhat more refined studies found that the rotation of the BH has a stabilizing effect [68,69], and a nonconstant radial profile angular momentum was found to strongly disfavor the instability [69–72]. On the other hand, studies using a Newtonian pseudopotential for the BH [73,74] and relativistic calculations with a fixed spacetime background [65,75] found indications of the self-gravity of the disk to favor the instability. However, Montero, Font, and Shibata [76] recently performed the first self-consistent and fully general-relativistic simulations of thick accretion disks around BHs in axisymmetry for a few dynamical time scales. They found no signatures of a runaway instability during the simulated time, perhaps implying that the self-gravity of the disk does not play a critical role in favoring the instability, at least during the first few dynamical time scales.

The problem of the existence and development of nonaxisymmetric instabilities has a long history. For thin Keplerian self-gravitating disks it was found that the Toomre parameter [77–79] can be used to determine stability against both local clumping or fragmentation, and formation of global nonaxisymmetric modes. For thick pressure-supported disks, Papaloizou and Pringle discovered [61] the existence of a global hydrodynamical instability that develops on a dynamical time scale in disks with negligible self-gravity and constant specific angular momentum. A follow-up publication [62] found this instability also in the disks with power law distribution of specific angular momentum $\ell(r) = \ell_0(r/r_c)^{2-q}$ for all $q > \sqrt{3}$. Kojima [63,80] found the Papaloizou-Pringle (PP) instability in equilibrium tori on a fixed Schwarzschild background [81] using a linearized perturbative approach.

Subsequent works clarified the nature of the PP instability [82–85], established how it redistributes specific angular momentum [86], and discovered that accretion has a stabilizing effect on the disk [87,88]. In particular, Goldreich, Goodman, and Narayan [82] showed that the PP modes are formed by two boundary wavelike perturbations with energy and angular momentum of opposite signs that are coupled across a forbidden region near the mode corotation radius. For wide disks around BHs, the accretion suppresses the development of the inner boundary wave and therefore has a stabilizing effect on PP modes [87,88]. For slender disks, the development of PP modes is mostly unaffected by accretion [88]. The PP instability itself amplifies accretion by exerting torques on the disk and redistributing specific angular momentum [86].

When the self-gravity of the disk has been taken into account, it was found [89–91] that two new types of nonaxisymmetric instabilities appear, while the PP instability disappears for most of the models except slender ones with weak self-gravity. The first type of unstable modes (J modes) appears in the strong self-gravity regime, and it is an analog of the classical Jeans instability. The second type of unstable modes was found in the strong and medium self-gravity regimes [89]. The modes of this type are referred to as intermediate modes (I modes) and represent elliptic deformations of the disk (or triangular, square, etc., deformations for higher azimuthal numbers—see, e.g., [91]).

Yet another type of instability, the so-called "eccentric instability," was discovered in [92] for thin nearly Keplerian self-gravitating disks when the central mass was allowed to move. An elaborate mechanism called "stimulation by the long-range interaction in Newtonian gravity amplification" [93] was proposed to describe this instability. Subsequent investigation [94] of this instability in thin disks suggested a different mechanism and predicted that the system is dynamically unstable only when the mass of the disk exceeds the mass of the central object.

Finally, Woodward, Tohline, and Hachisu [64] presented an extensive parameter study of thick self-gravitating disks in Newtonian gravity to determine the types, growth rates, and pattern speeds of nonaxisymmetric modes. The central mass in their simulations was allowed to move, and they used 3D time evolutions of the disk models with a wide range of parameters, including disk-to-central object mass ratios $M_D/M_c = 0$, 1/5, 1, and ∞.

Several recent publications address accretion disks and instabilities in these disks in the context of GRB central engines. In [20], Rezzolla *et al.* studied the properties of accretion disks resulting from binary NS mergers. They obtained thin accretion disks with masses $\sim 0.01\text{–}0.2\mathcal{M}_\odot$ and no evidence of growing nonaxisymmetric modes or runaway instability. In [95], Taylor, Miller, and Podsiadlowski used 3D smoothed-particle hydrodynamics simulations with detailed microphysics and neutrino transport to follow a collapse of an iron core up to the formation of a thin massive accretion disk and development of global nonaxisymmetric modes. They found that torques created by the nonaxisymmetric modes provide the main mechanism for angular momentum transport, leading to high accretion rates of $\sim 0.1\text{–}1\mathcal{M}_\odot/\mathrm{s}$, which may create favorable conditions for powering GRBs.

The stability of disks to runaway and nonaxisymmetric instabilities is a three-dimensional problem that has to be addressed in the framework of full general relativity (GR). One issue of importance is to understand if the runaway instability is affected by nonaxisymmetric instabilities, and vice versa. Despite significant theoretical and computational effort, previous studies of the runaway instability do not give a definite answer to this question. To our knowledge, only the work by Rezzolla *et al.* [20] explored the stability of the disks in 3D and full GR (for the disks that form in their binary NS merger simulations). However, it is important to create a comprehensive overall picture of the stability of accretion disks for a richer variety of disk models, which would require investigating a wider range of parameters. In our work, we study in detail the stability of slender and moderately slender disks with constant distribution of specific angular momentum, which are expected to be more unstable to nonaxisymmetric instabilities [87,88] compared to models of Rezzolla *et al.* [20], and potentially unstable to the runaway instability [70,71]. Our study is based on three-dimensional hydrodynamics simulations in full GR.

We model our disks using the ideal fluid approximation (i.e. without viscosity) with a Γ-law equation of state (EOS) and $\Gamma = 4/3$. We do not include additional physics such as magnetic fields or neutrino and radiation transport due to the complexity and computational cost of the resulting problem. Nevertheless, the adopted approach will allow us to identify GR effects which can operate in a more complex setting that include more realistic microphysics, neutrino and radiation transport, and magnetic fields. Also, we limit ourselves to the case of nonrotating BHs, while the case of rotating BHs will be studied in future publications.

Another aim of this paper is to estimate the detectability of the gravitational waves (GWs) by the accretion disk dynamics. The radial and/or nonaxisymmetric oscillations of accretion disks can be a source of strong GWs. If nonaxisymmetric deformations persist for a long enough time, then the emitted GWs can be detectable by current and future GW detectors [96], provided the source is not too far away. Further work on the stability properties of the accretion disk could shed more light on the number of cycles a nonaxisymmetric deformation can persist and thus on the prospects of detecting GWs from such systems.

This paper is organized as follows: Section II describes the formulations and numerical methods used in this paper, including multiblock grids (Sec. II A) and the formulations used to evolve the general-relativistic (Sec. II C) and hydrodynamic (Sec. II B) equations. Section III describes the grid setup, initial data construction procedure, and the analysis techniques for the nonaxisymmetric instabilities. Sections IV and V present the results of the time evolution of self-gravitating disks and the analysis of nonaxisymmetric instabilities.

Throughout the paper we use the centimeter-gram-second (CGS) system and geometrized units $G = c = 1$.

II. NUMERICAL METHODS

The numerical time-evolution scheme used in our study can be split into two main parts: the spacetime evolution and the fluid dynamics equations. These two parts are evolved in a coupled manner. The numerical code that we use has been developed within the CACTUS computational infrastructure [97,98] and uses the CARPET mesh refinement and multiblock driver [99,100]. A separate module based on CARPET provides a range of multiblock systems to represent a variety of computational domains for 3D evolution codes [101]. The module for evolving the GR hydrodynamics equations uses the THOR multiblock code [102], which has been coupled to the multiblock-based module QUILT for evolving the spacetime [103]. The latter implements the generalized harmonic formulation of the Einstein equations in first-order form [104]. Below, we give a brief description of the methods implemented in each module.

A. Multiblock approach

For mesh generation and parallelization purposes, we employ the multiblock infrastructure developed by [101]. The multiblock approach is widely used in astrophysical and numerical relativity simulations (see [36,105–123], and references therein).

Figure 1 shows meridional cuts (cuts in the xz plane) of the block systems that we use. The first two block systems in Fig. 1 are the seven-block (also known as a "cubed sphere" [124]) and the 13-block systems. They both have a spherical outer boundary and no coordinate singularities. The 13-block system additionally has spherical grid coordinate surfaces in the outer layer of blocks, which is very convenient for computing spherical harmonics and extracting gravitational waves. The 13-block system is well adapted for simulating processes that involve a small

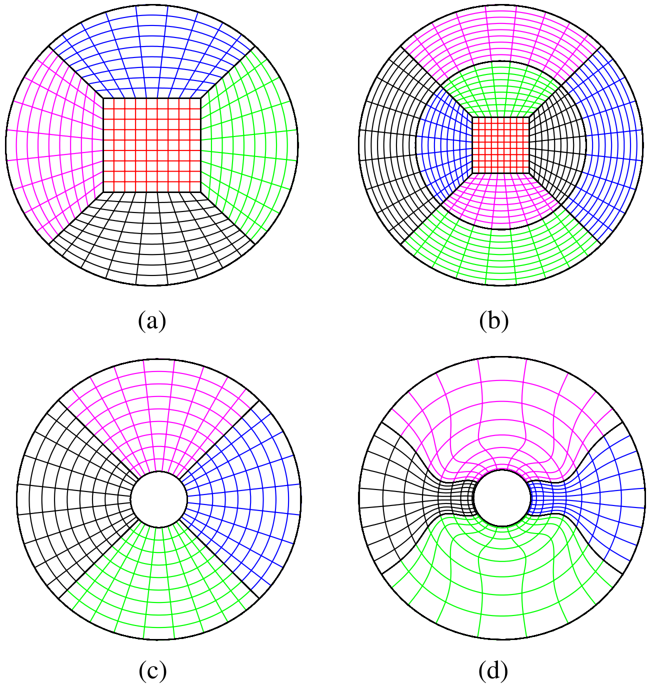

FIG. 1 (color online). Cross sections of the patch systems used in this work in the xz plane: (a) seven-block system; (b) thirteen-block system; (c) six-block system with straight coordinate lines; (d) six-block system with distorted radial coordinate lines, described in Sec. III C below.

source of waves, surrounded by an extended spherical wave propagation region. The central cubical block can have a high resolution and can be used to model accurately the dynamics of the source and the intermediate layer can represent a near zone, while the outer layer of blocks model the radiation zone, which can carry an outgoing radiation using, e.g., constant angular and radial resolutions. These two systems are used in the appendix for test evolutions of rotating and nonrotating polytropic stars.

The remaining block systems in Figs. 1(c) and 1(d) are six-block systems, and these systems are more suitable for modeling configurations with a central black hole. The block system displayed in Fig. 1(d) is similar to the block systems that we use for simulating accretion disks around black holes (see Sec. III C). These two block systems contain an empty spherical region, which is used for excising the interior of the BH.

The multiblock approach has a number of additional advantages, including a smooth excision boundary [115,125,126], a smooth spherical outer boundary suitable for radiating boundary conditions, a spherical wave propagation zone, and the absence of coordinate singularities such as those associated with spherical or cylindrical coordinates. Also, multiblock systems such as displayed in Fig. 1 allow one at low cost to extend the computational domain far outwards in order to, e.g., causally disconnect the system dynamics from the outer boundary and to allow more accurate extraction of gravitational waves [103,127].

B. Hydrodynamics evolution

The evolution equations of a relativistic fluid are derived from the covariant equations of conservation of rest mass $\nabla_a(\rho u^a) = 0$ and energy momentum $\nabla_b T^{ab} = 0$, where T^{ab} has the following form for an ideal fluid [102,128]:

$$T^{ab} = (\rho + u + P)u^a u^b + P g^{ab},$$

where P is the fluid pressure, ρ is the rest-mass density, u is the internal energy density,[3] u^a is the fluid's four-velocity, and g^{ab} is the spacetime metric in contravariant form. The quantities $\{\rho, u^i, u\}$ form a set of *primitive variables* that uniquely determine the state of a single-component relativistic fluid at every point in space.

Our evolution equations read

$$\partial_t(\sqrt{-g}\rho u^t) + \partial_i(\sqrt{-g}\rho u^i) = 0,$$
$$\partial_t(\sqrt{-g}T^t{}_a) + \partial_i(\sqrt{-g}T^i{}_a) = \sqrt{-g}T^c{}_d\Gamma^d{}_{ac},$$

where t is the time coordinate, $g \equiv \det(g_{ab})$ is the determinant of the spacetime metric, and $\Gamma^d{}_{ac}$ are the Christoffel symbols associated with this metric. After introducing a set of *conserved variables* $\{D \equiv \sqrt{-g}\rho u^t$, $Q_a \equiv \sqrt{-g}T^t_a\}$, the equations can be cast into a flux-conservative form (as in [131,132]; see details specific to our particular scheme in [102]):

$$\partial_t D + \partial_i D^i = 0, \qquad \partial_t Q_a + \partial_i Q^i_a = S_a,$$

where D^i and Q^i_a are the fluxes of the conserved variables D and Q_a, respectively, while S_a are the source terms for Q_a.

These equations are solved on each block using a finite volume cell-centered scheme in the local coordinate basis of that block. The reconstruction of the primitive variables on the cell interfaces is performed using the piecewise-parabolic monotonous method [133,134], while the fluxes through the interfaces are calculated using a Harten-Lax-van Leer Riemann solver [135]. In order to compute fluxes, source terms, and the stress-energy tensor T^{ab}, the conservative variables need to be converted into primitive ones at every time step. This is done using a Newton-Rhapson iterative $2D_W$ solver [136] with the nonisentropic Γ-law EOS. If at a particular cell on the grid the procedure of primitive variables recovery fails to produce physically meaningful values (which can happen for a number of reasons; see, e.g., [136]), we use a $1D_P$ solver with an isentropic polytropic EOS. The vacuum region outside the disk is approximated by a low-density artificial atmosphere, whose density is chosen to be 10^{-6}–10^{-7} of the initial maximum density in the system.

The boundary conditions for the hydrodynamics variables are imposed on the interblock boundaries using interpolation from neighboring blocks. The overlap regions

---

[3] It is also common to define a specific internal energy $\varepsilon = u/\rho$ [129,130].

where interpolation is performed are created by adding extra layers of grid points on each block face. At the outer boundary and the inner excision boundary, we impose outflow boundary conditions. Further details on this numerical method of combining multiple blocks can be found in [102].

C. Spacetime evolution

To evolve the spacetime metric g_{ab} we use a generalized harmonic formulation of the Einstein equations in the first-order representation developed by Lindblom *et al.* [104]. In this formulation, the coordinate conditions are specified using a set of four gauge source functions H_a, which need to be prescribed *a priori*. In our simulations, we have chosen the so-called "stationary gauge" [104,137], in which the gauge source functions stay frozen at their initial values, $H_a(t, x^i) = H_a(t_0, x^i)$. Such a choice of the gauge is convenient for quasistationary spacetimes, such as perturbed BHs [103] or accretion disks around BHs.

The first-order representation that we use is linearly degenerate, symmetric hyperbolic [138–140], and constraint damping. Linear degeneracy guarantees that the system will not develop gauge shocks during the evolution [141]. Symmetric hyperbolicity with boundary conditions imposed on incoming characteristic fields is the necessary condition for well-posedness of initial boundary value problems (see, e.g., Chap. 6 of Gustafsson, Kreiss, and Oliger [142]).

Being constraint damping, which is one of the most important advantages of the chosen formulation, means that the constraints on the variables are included into the evolution equations in such a way that they are exponentially damped during evolution. Such a property not only reduces the error in the solution but also eliminates a variety of numerical instabilities associated with unbounded growth of the constraints.

The spacetime metric evolution equations are discretized using finite differences on multiple grid blocks that cover the computational domain [101,102]. This means that the spacetime grid blocks are only subsets of the hydrodynamics grid blocks; the overlap regions where the hydrodynamics variables are interpolated are absent in the spacetime grid blocks. The advantages of using multiple blocks were outlined in Sec. II A above. The grids on any two neighboring blocks in the system are designed to share a 2D interface grid, where so-called penalty boundary conditions are imposed [143]. For the spatial numerical differentiation, we employ high-order convergent finite-differencing operators that satisfy the summation by parts property [144]. The summation by parts property together with penalty boundary conditions guarantees strict linear numerical stability [143]. All simulations of self-gravitating disks with dynamical treatment of relativistic gravity in the paper were performed with the finite-differencing operators of eighth-order convergence in the bulk of the grid and fourth-order convergence at the boundaries. Time integration is performed with a third-order accurate Runge-Kutta method that satisfies a total variation diminishing property [145].

D. Code tests

Numerical methods for solving the general-relativistic hydrodynamics equations and the spacetime equations are inherently complex, and codes need to be thoroughly tested before they can be successfully applied to physical problems (see, e.g., [146,147]). The hydrodynamics code THOR was tested for fixed spacetimes by Zink, Schnetter, and Tiglio in [102], where it was demonstrated that the code can handle situations encountered in many astrophysical scenarios, including relativistic shocks, rotating polytropes, and equilibrium tori around BHs [81]. The spacetime evolution code QUILT was tested in [103,148].

We present results of our tests of the coupled hydrodynamics and spacetime evolution codes in the appendix, Secs. 2 and 3. In particular, in Sec. 2 we report stable convergent evolutions of a rapidly rotating polytropic star, and in Sec. 3, we demonstrate that our code faithfully reproduces fundamental frequencies of a nonrotating polytropic star. Additionally, recently Zink *et al.* [149] have used the coupled Thor + Quilt code to measure the frequencies of f modes and to study their neutral points in the context of the Chandrasekhar-Friedman-Schutz instability.

E. Constraint damping

The constraint damping scheme for the spacetime evolution mentioned above depends on two freely specifiable parameters: κ and γ_2. These parameters can be freely chosen as a function of space and time; i.e. the system of equations does not directly depend on their spatial or temporal derivatives. Here we describe how these parameters are specified in our simulations.

In the generalized harmonic formulation, the set $u^\alpha = \{g_{ab}, \Phi_{iab}, \Pi_{ab}\}$ of dynamical fields consists of the metric g_{ab} and linear combinations of its derivatives $\Phi_{iab} = \partial_i g_{ab}$, $\Pi_{ab} = -n^c \partial_c g_{ab}$, where n^c is a normal to a $t =$ const hypersurface. The evolution equations for the fields can be written in the following form:

$$\partial_t g_{ab} = G_{ab}(x^a, u^\alpha), \tag{1}$$

$$\partial_t \Phi_{iab} = \mathcal{F}_{iab}(x^a, u^\alpha) - \gamma_2 C_{iab}, \tag{2}$$

$$\partial_t \Pi_{ab} = P_{ab}(x^a, u^\alpha) - \kappa C_{ab} - \gamma_2 \beta^i C_{iab}, \tag{3}$$

where C_{ab} and C_{iab} are the constraints, β^i is the shift vector, and G_{ab}, $\mathcal{F}_{iab}$, and P_{ab} are right-hand sides of the formulation *without* the constraint damping terms. In the continuum limit, the constraints are zero, and the system (3) reduces to the original Einstein equations. At the discrete level, the constraints can be nonzero, and the constraint damping terms provide a nonvanishing contribution to the right-hand sides of the system (3).

Since constraint damping terms should act only as small corrections to the evolution system, their contribution should not exceed those of functions G_{ab}, $\mathcal{F}_{iab}$, and P_{ab}. Otherwise, the evolution of the system will be dominated by the numerical constraint violations.

We notice in our simulations that the functions $\mathcal{F}_{iab}$ and P_{ab} on the right-hand sides of (1) fall off as $1/r^\alpha$ with $\alpha \sim 4$ beyond $r > r_{\rm disk}$, where $r_{\rm disk}$ is the approximate outer radius of the disk. At the same time, the constraint violations C_{ab} and C_{iab} fall off as $1/r^\beta$ with $\beta \sim 1$. This means that, if we use constant values for γ_2 and κ, the constraint damping terms will dominate the dynamics of the system for sufficiently large r. In order to avoid this situation, the functions κ and γ_2 must fall off with the radius as $\sim 1/r^3$.

We find that the following radial profiles of κ and γ_2 for our simulations lead to satisfactory results:

$$\kappa(r) = \kappa_*\left[1 - \frac{2}{\pi}\left(\frac{r_*}{1 + r_*^2} + \arctan r_*\right)\right], \tag{4}$$

$$\gamma_2(r) = \gamma_*\left[1 - \frac{2}{\pi}\left(\frac{r_*}{1 + r_*^2} + \arctan r_*\right)\right], \tag{5}$$

where $r_* = (r - r_0)/\sigma$ and κ_*, γ_*, r_0, and σ are (positive) constants. This radial profile approaches a constant value of $\sim\kappa_*$ (or $\sim\gamma_*$) for $r < r_0$ and falls off as $\sim 1/r^3$ for $r \gg r_0$. The parameter σ determines the extent of the smooth transition region between these two regimes. We use $\kappa_* = \gamma_* = 4$, $r_0 = 12$, and $\sigma = 8$ in our simulations. Such profiles of the constraint damping coefficients allows imposing strong constraint damping near the BH and the disk without introducing spurious dynamics far away from the origin.

III. INITIAL SETUP

We set up initial equilibrium disk configurations by solving Einstein constraints using a version of the RNS solver [150] adapted to the problem of equilibrium tori. The method of solution is similar to the one used in [151]. The spacetime is assumed to be stationary, axisymmetric, asymptotically flat, and symmetric with respect to reflections in the equatorial plane. The metric is a general axisymmetric metric in quasi-isotropic coordinates:

$$ds^2 = -\lambda^2 dt^2 + e^{2\alpha}(dr_*^2 + r_*^2 d\theta^2) \tag{6}$$

$$+ B^2/\lambda^2 r_*^2 \sin^2\theta (d\varphi - \omega dt)^2, \tag{7}$$

where $(t, r_*, \theta, \varphi)$ are the coordinates and λ, α, B, and ω are metric potentials which depend only on r_* and θ. The RNS code implements the Komatsu-Eriguchi-Hachisu (Stergioulas-Friedman) method [150,152], in which the Einstein equations for the metric potentials λ, B, and ω are transformed into integral equations [151] using Green's functions for the elliptical differential operators. The remaining metric potential α can then be found by integrating an ordinary differential equation, once the rest of the potentials are known. The Komatsu-Eriguchi-Hachisu (Stergioulas-Friedman) method uses compactified radial coordinate s which maps the region $[0, \infty)$ into a segment $[0, 1]$:

$$s \equiv \frac{r}{r + r_+},$$

where r_+ is the outer radius of the disk. The boundary conditions are imposed at symmetry interfaces and at the event horizon. The latter can always be transformed to a sphere of compactified radius s_h, while preserving the form of the metric given above [151]. At the horizon, we impose the boundary conditions for a nonrotating BH: $\lambda = B = \omega = 0$, and we set $B/\lambda = e^\alpha$ at the symmetry axis. The corresponding integral equations are then solved using Newton-Raphson iterations [150] in the upper quadrant $\theta \in [0, \pi/2]$, $s \in [0, 1]$ of the meridional plane.

The resulting quasi-isotropic metric is degenerate at the event horizon, which is very problematic for the evolution with excision of the BH interior using the generalized harmonic formulation, since this method requires coordinates without pathologies at the event horizon. This situation is best illustrated by a conformal picture of the complete spacetime, shown in Fig. 2. All quasi-isotropic slices meet the horizon of the BH at its throat, which makes the metric degenerate at the horizon. Regions II and IV are not covered by the quasi-isotropic foliation. It is necessary for our time-evolution methods to have a time-independent foliation which penetrates the horizon and continues in region II rather than region III.

There are several options to address this issue:

1. solve the complete system of equations in horizon-penetrating coordinates rather than quasi-isotropic ones;
2. use puncture initial data, as developed in [153], and choose such a gauge for the evolution that after some time the spatial slices move from region III

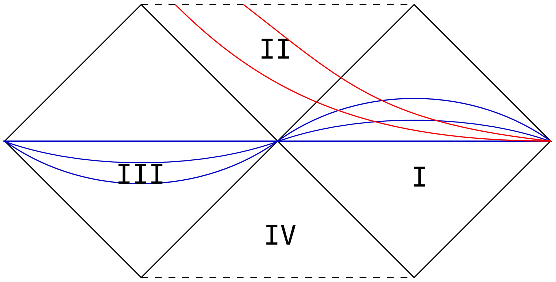

FIG. 2 (color online). Conformal Penrose diagram of an axisymmetric spacetime, consisting of a nonrotating BH, distorted by a massive stationary disk around it. Each point on the diagram corresponds to a spheroid, located at a given geodesic distance from the BH horizon. Blue lines represent a quasi-isotropic foliation of the spacetime, while red lines show a horizon-penetrating foliation.

to region II, similarly to what happens with punctures in the Baumgarte-Shapiro-Shibata-Nakamura formulation and 1 + log slicing [154];

(3) apply a spacetime coordinate transformation from quasi-isotropic to horizon-penetrating coordinates. Since there is still no solution provided in region II, it needs to be extrapolated into that region.

We use option (3), since it is easier to implement in the context of the generalized harmonic system and fits more naturally in the gauge choice employed by RNS. Details on the spacetime transformation that we apply to the initial data can be found in the appendix.

A. Blending numerical and analytical metrics

We could not extrapolate the initial data produced by the elliptic solver to region II inside the horizon, because the data do not have enough smoothness near the horizon. The problem with the initial data at the horizon seems to be similar to the problem with Gibbs phenomena, when solutions exhibit an oscillatory behavior and a lower order of convergence near a stellar surface. To handle this problem, we use an approximation, in which we replace the numerical metric in the region where it is not accurate with an analytic Kerr-Schild solution of the same BH mass. We blend the numerical metric g_{ab}^{num} and the Kerr-Schild metric g_{ab}^{KS} using the following prescription:

$$g_{ab} = (1 - w(r))g_{ab}^{\mathrm{num}} + w(r)g_{ab}^{\mathrm{KS}},$$

where the weight function $w(r)$ is defined as

$$w(r) = \begin{cases} 1, & \text{if } r < b_1, \\ \cos^2 \frac{\pi(r-b_1)}{2(b_2-b_1)}, & \text{if } r \in [b_1, b_2], \\ 0, & \text{if } r > b_2, \end{cases}$$

and the segment $r \in [b_1, b_2]$ determines a finite-size blending zone between the two metrics. The weight function $w(r)$ is nonconstant only in a narrow spherical layer outside the horizon.

Blending two metrics introduces constraint violations at the continuum level, but they subside rapidly in time due to the constraint damping property of our evolution scheme. The constraint damping scheme, however, does not necessarily satisfy the conservation of mass, so after the constraint violations are suppressed, the system arrives at a different state, which can be characterized as a close equilibrium configuration with some axisymmetric gravitational perturbation.

The location and size of the blending layer can be adjusted to minimize the initial unphysical oscillation in a BH mass. For the evolutions presented below, we used blending in the range $r \in [1.05r_g, 1.15r_g]$, where r_g is the radius of the BH event horizon. Such a choice results in the initial oscillation of the BH mass within $\approx 12\%$, which then settles down to a stationary value of $(97.5 \pm 0.5)\%$ during the first orbital period [see Fig. 8(b) and related discussion in Sec. IV].

B. Initial disk models

We have constructed three initial disk models with disk-to-BH mass ratios $M_D/M_{\mathrm{BH}} = 0.235$, 0.174, and 0.108, labeled A, B, and C, respectively. Model C is slender, which

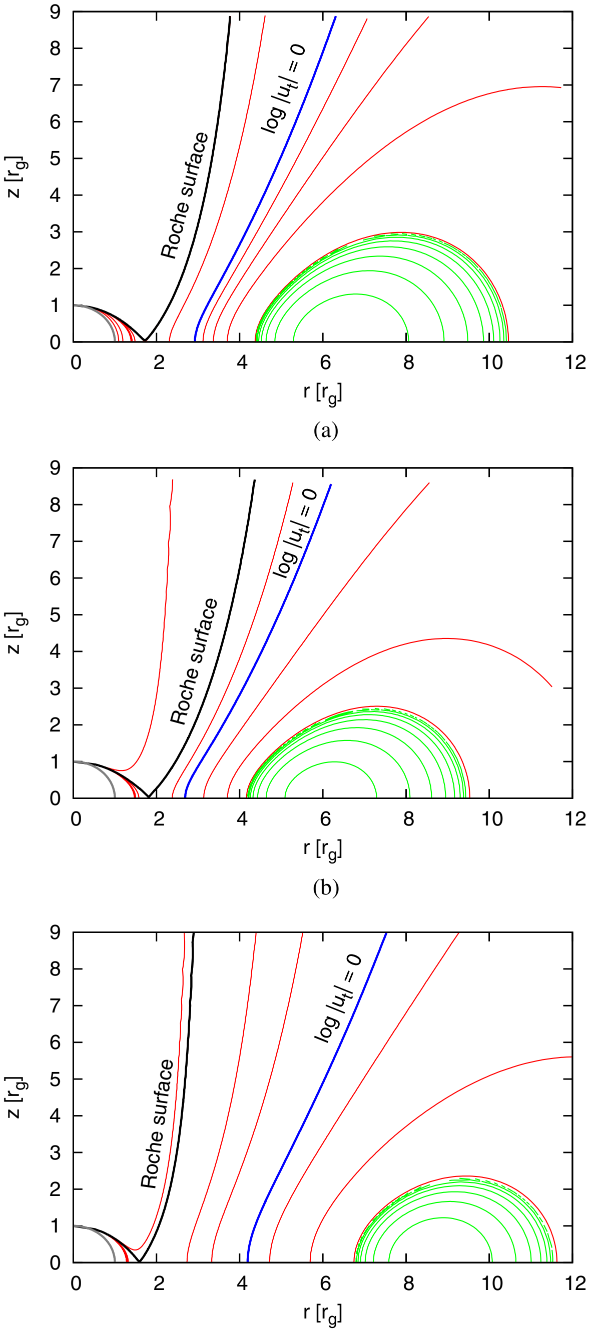

(a)

(b)

(c)

FIG. 3 (color online). Geometry of the initial disk models A (top), B (middle), and C (bottom). Green lines represent the contours of equal density, while red lines represent the contour plots of $W = \log|u_t|$ (as introduced in Sec. III B). The latter quantity plays the role of the effective potential. The plots also show the location of the Roche surface (thick black line) and the last bound surface $\log|u_t| = 0$ (thick blue line).

TABLE I. Physical parameters of the self-gravitating initial disk models, used in our simulations.

Model	A	B	C
Specific angular momentum $\ell[M_{\rm BH}]$	4.50	4.32	4.87
Polytropic constant $K[10^{14}\ {\rm cm}^3\ {\rm g}^{-1/3}\ {\rm s}^{-2}]$	1.28	1.04	0.519
Maximum density $\rho_c[10^{13}\ {\rm g/cm}^3]$	1.23	1.17	0.755
Disk-to-BH mass ratio $M_D/M_{\rm BH}$	0.235	0.174	0.108
Kinetic to potential energy $T/\lvert W\rvert$	0.479	0.497	0.499
Central radius r_c/r_g	6.51	6.10	8.75
Inner radius r_-/r_g	4.26	4.17	6.74
Ratio of inner to outer radius r_-/r_+	0.385	0.438	0.580
Radial location of the cusp r_L/r_g	1.72	1.81	1.59
Orbital frequency at r_c, $\Omega_c[{\rm s}^{-1}]$	1713	1912	1121
Self-gravity parameter $\tau = 4\pi G\rho_c/\Omega_c^2$	3.52	2.68	5.04

means that its width is much smaller than the radius of the torus, i.e. $r_c \gg r_+ - r_-$. Models A and B are moderately slender, i.e. for these models $r_c \approx r_+ - r_-$. Figure 3 shows the contour plots of the disk density in a meridional plane along with the quantity $W \equiv \log|u_t|$, which plays the role of the effective potential [81] in axisymmetric equilibrium configurations (here u_t refers to the specific energy of a test particle on a circular orbit with given specific angular momentum ℓ). Notice that since the last bound surface $W = 0$ is located between the disk and the Roche lobe, the latter is open in all three models. Therefore, for these models the high angular momentum prevents the runaway instability and the small amount of accretion is not sufficient to change this situation. This situation cannot be changed unless there is a significant amount of accretion. All models are constructed using a polytropic EOS with polytropic index $\Gamma = 4/3$, constant specific entropy, and a constant specific angular momentum distribution.

Table I lists physical and geometrical parameters of the disk, including the ratio of disk-to-BH mass $M_D/M_{\rm BH}$, radial location of the cusp in equipotential surfaces r_L, the ratio of kinetic energy T to potential energy W, and the self-gravity parameter τ. The latter can be defined as $\rho_c/\rho_{\rm sph}$, where $\rho_{\rm sph} \equiv \Omega_c^2/4\pi G$ is the density of a uniform sphere with radius r_c that creates equivalent gravity at that radius. Notice that $T/|W|$ correlates to the "slenderness" of the disk r_-/r_+. Also notice that in models A and B the distance from the inner edge of the disk to the cusp ($\sim 2.5 r_g$) is smaller than that in model C ($\sim 5 r_g$). This makes the development of the runaway instability more unlikely for model C (see Fig. 3). The value of specific angular momentum ℓ is given in units of the BH mass. These parameters allow us to make qualitative and quantitative comparisons between our models and the models studied in previous works [64,89–91,155].

C. Adapted curvilinear grid

In order to accurately resolve both the disk and the BH while minimizing the computational cost, we have designed a series of curvilinear multiblock grids adapted to each of the disk models. To obtain such a grid, we start from a six-block system [displayed in Fig. 1(c)] that was previously used in QUILT for computationally efficient and numerically accurate simulations of perturbed BHs [103]. We apply a radial stretching and an angular distortion to the six-block system so as to create a uniformly high resolution near the BH, nearly cylindrical grid near the disk, and approach a regular six-block spherical grid in the wave zone. These mappings are described in detail below. Figure 1(d) shows an illustration of the grid distortion, while Fig. 4(a) shows the actual curvilinear grid used in some of our simulations.

A regular six-block system consists of two polar blocks (near the z axis) and four equatorial blocks (near the xy plane). We can assign quasispherical coordinates $\{r, \theta, \varphi\}$ and $\{r, \theta_1, \theta_2\}$ to the equatorial and polar blocks, respectively. They can be related to the Cartesian coordinates $\{x, y, z\}$ by the following transformation:

(i) For an equatorial block in the neighborhood of the positive x axis,

$$x = r/\sqrt{1 + \tan\varphi^2 + \tan\theta^2},$$
$$y = x\tan\varphi,$$
$$z = x\tan\theta,$$

(ii) while for a polar block in the neighborhood of the positive z axis,

$$x = z\tan\theta_1,$$
$$y = z\tan\theta_2,$$
$$z = r/\sqrt{1 + \tan\theta_1^2 + \tan\theta_2^2}.$$

(iii) The remaining blocks are obtained by applying symmetry transformations.

We set the coordinate ranges for the polar blocks to be $r \in [R_{\rm min}, R_{\rm max}]$, $\theta_1, \theta_2 \in [-\theta_*, \theta_*]$, where the value of θ_*

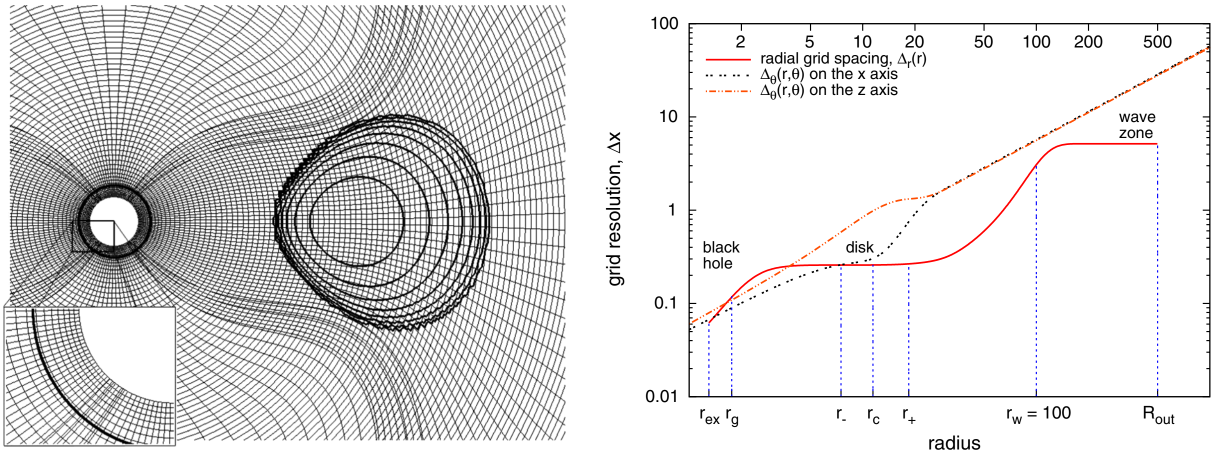

(a) (b)

FIG. 4 (color online). Left panel (a): Meridional cut of an adapted curvilinear grid used in one of our simulations, combined with the logarithmic density contours of the disk at $t = 0$. The intersecting radial coordinate lines belong to the neighboring blocks in the overlapping (interpolated) regions. The thick black circle marks the location of an apparent horizon of the BH. The inset in the lower left corner of the plot shows the high-resolution grid around the BH, adapted in such a way that the resolution is uniformly high in every direction. Right panel (b): Radial profile of the resolution in the r (red solid line) and the θ (dotted lines) directions for the grid shown in the top panel. The radial coordinate is plotted in the logarithmic scale. The top horizontal axis shows the values of the radius in numerical units. The marks on the lower axis are $r_{\rm ex}$ is the radius of the BH excision sphere; r_g is the gravitational radius of the BH; r_- and r_+ are the inner and outer radii of the disk, respectively; r_c is the radius of the density maximum; r_W is the "wave extraction" radius; $R_{\rm out}$ is the outer radius of the domain. The black dotted line is the resolution in the θ direction on the x axis, and the red dash-dotted line is the resolution in the θ direction on the z axis.

controls an opening angle of the polar blocks. For equatorial blocks, $r \in [R_{\rm min}, R_{\rm max}]$, $\theta \in [-\frac{\pi}{2} + \theta_*, \frac{\pi}{2} - \theta_*]$, and $\varphi \in [-\frac{\pi}{4}, \frac{\pi}{4}]$. The size of the numerical grid for each block is fixed by three numbers: N_r, N_φ, and N_θ. The equatorial blocks have $N_r \times N_\varphi \times N_\theta$ cells, and the polar ones have $N_r \times N_\theta \times N_\theta$ cells.

In order to obtain a variable radial resolution, we apply a smooth one-dimensional radial stretching S: $r \to \bar{r}$ that yields the desired resolution profile $\Delta_r(r)$. This profile is chosen based on several stringent requirements imposed by an accuracy and available computational resources. First, there need to be at least 8 grid points between the excision radius and the BH horizon in order to prevent constraint violations from leaving the interior of the BH (this question is considered in some detail in [156]), as well as to allow for some (restricted) BH movement. Second, our convergence tests show that near the disk, the grid needs to allow for at least 40 points across the disk in order to achieve a global convergent regime in hydrodynamical evolutions. For this purpose, the radial resolution profile is adapted to have sufficiently high resolution near the disk as well. Third, in the wave zone, there is no need to maintain very high radial resolution. However, this resolution needs to be uniform (rather than, for example, exponentially decreasing) to be able to carry the radiation accurately without dissipation. All these requirements result in the radial resolution profile $\Delta_r(r)$ shown in Fig. 4(b).

The resolution in the θ direction Δ_θ near the disk also needs to have at least 40 points across the disk for convergence. However, a simple increase of N_θ in the six-block system leads to a very small minimal grid step $\Delta_{\rm min}$ at the excision radius $R_{\rm min}$ that is too restrictive for the time step due to the Courant factor limit condition. To increase the grid resolution in the θ direction near the disk only, we apply a radial-dependent distortion to the angular coordinates θ, θ_1, and θ_2:

$$\theta(\bar{\theta}, r) = \bar{\theta}\left(1 - \beta(r)\frac{\cos 2\theta_*}{\pi - 2\theta_*}\right),$$

$$\theta_i(\bar{\theta}_i, r) = \bar{\theta}_i\left(1 + \beta(r)\frac{\sin 2\theta_*}{2\theta_*}\right), \qquad i = 1, 2,$$

where the function $\beta(r)$ is the amplitude of the distortion, chosen to have a Gaussian profile $\beta(r) = \beta_* \exp(-(r - r_0)^2/\sigma^2)$, in which the parameters β_*, r_0, and σ are chosen to satisfy the above requirements. This distortion bends diverging radial coordinate lines towards the equatorial plane around the radius r_0, making the grid resemble a cylindrical shape near that radius [as illustrated by Fig. 4(a)]. Figure 4(b) shows the dependence of Δ_θ on r along the x axis (dotted black line) and along the z axis (dash-dotted red line). The radial-dependent θ distortion increases Δ_θ on the x axis at the expense of Δ_θ on the z axis near the disk. Away from the disk, the distortion vanishes and Δ_θ approaches the linear dependence $\Delta_\theta(r) \propto r$.

Figure 4 shows an example of the resulting curvilinear grid. For this example, $\theta_* = 30°$, $N_\theta = 49$, and $N_\varphi = 25$. These parameters make the grid spacing approximately uniform in the angular direction near the BH and at large r. The inner (excision) radius is $R_{\mathrm{min}} = 1.3$ and the outer one is $R_{\mathrm{max}} = 500$, while the minimum grid spacing is $\Delta_{\mathrm{min}} = \Delta_\theta(r_{\mathrm{min}}) \approx 0.06$. The apparent horizon has a radius of ≈ 1.7, so that as many as 8 grid points can be placed inside the horizon without decreasing the minimum grid spacing. Distortion parameters of the Gaussian have values $r_0 = 12$, $\sigma = 8$, and $\beta_* = 1.3$, which is sufficient to concentrate about 40 grid points across the disk in the vertical direction. The radial resolution is adapted to be $(\Delta_r)_{\mathrm{BH}} \approx 0.06$ at the excision sphere, $(\Delta_r)_{\mathrm{disk}} \approx 0.25$ around the disk, and $(\Delta_r)_{\mathrm{WZ}} \approx 5.2$ in the wave zone.

All of the time evolutions described in the next two sections IV and V use adapted six-block curvilinear grids. Table II summarizes dimensions and resolutions of the grids for each of the simulations used in these two sections. The first column lists simulation names, which consist of two or three symbols. Models K1–K6 are considered in Sec. VA. In the rest of the model names, the first letter denotes the initial disk model (A, B, or C), and the second letter signifies whether the simulation is evolved in the full GR (F) or the Cowling (C) approximation (see corresponding Secs. V C and V B). The next number (if present) is the azimuthal number m of an added nonaxisymmetric perturbation (as explained in Sec. V). Simulations AFc, AF, and AFf represent disk model A evolved in full GR using coarse, medium, and fine resolution grids, respectively. These models are used in Sec. IV for convergence studies. Finally, note that the adapted curvilinear grid example above (displayed in Fig. 4) corresponds to the grid used in simulation AF, and the grids of simulations AFf and AFc are obtained by increasing and decreasing, respectively, the resolutions in the AF grid by a factor of 3/2.

D. Data analysis

To identify and characterize nonaxisymmetric instabilities, we will adopt an approach commonly used in linear perturbative studies of accretion disks (e.g., in [64,80]). Namely, we analyze the first few terms in the Fourier expansion in angle φ of the disk density $\rho(r, \varphi)$ on a sequence of concentric circles in the equatorial plane:

$$\rho(t, r, \varphi) = \bar{\rho}(t, r)\left(1 + \sum_{m=1}^{\infty} D_m e^{-i(\omega_m t - m\varphi)}\right),$$

where $\bar{\rho}$ is a φ-averaged density at a given radius. The quantity D_m represents the (complex) amplitude of an azimuthal mode m, and the real part of the quantity ω_m determines a mode pattern speed, while its imaginary part determines a mode growth rate. Following [64,157], we quantify the growth rate and the pattern speed of a nonaxisymmetric mode by two dimensionless parameters y_1 and y_2, defined as

$$y_1(m) = \frac{\mathrm{Re}(\omega_m)}{\Omega_{\mathrm{orb}}} - m, \qquad y_2(m) = \frac{\mathrm{Im}(\omega_m)}{\Omega_{\mathrm{orb}}}.$$

We calculate a value of the parameter $y_2(m)$ from a slope of $\log|D_m|$ versus t line at an arbitrary radius, while $y_1(m)$ is obtained from a slope of the mode phase angle $\varphi_m = \varphi_m(t)$. Notice that because the modes that we consider

TABLE II. Parameters of numerical grids for all the simulations of accretion disks used in this study. The naming convention of the simulations is explained in the main text in Sec. III C on adapted curvilinear grids. All resolutions and linear dimensions are given in computational units. The first column, which lists the values of the BH gravitational radius r_g, allows one to convert all quantities from computational to CGS units. The remaining columns contain: R_{min} and R_{max} are radial extents of the computational domain; N_x is the number of grid points in the horizontal x or y direction; N_z is the number of grid points in the vertical direction; N_r is the number of grid points in the radial direction; Δ_{min} is the minimal grid step size, in the θ direction at the excision sphere; $(\Delta_r)_{\mathrm{disk}}$ is the resolution in the r direction at radius r_c; $(\Delta_\theta)_{r_c,x}$ is the resolution in the θ direction on the x axis at radius r_c; $(\Delta_\theta)_{r_c,z}$ is the resolution in the θ direction on the z axis at radius r_c; $(\Delta_r)_{\mathrm{WZ}}$ is the radial resolution in the wave zone (not used for simulations on a fixed background).

Model	r_g	R_{min}	R_{max}	$N_x \times N_z \times N_r$	Δ_{min}	$(\Delta_r)_{\mathrm{disk}}$	$(\Delta_\theta)_{r_c,x}$	$(\Delta_\theta)_{r_c,z}$	$(\Delta_r)_{\mathrm{WZ}}$
K1	2.0	4.0	30	$25 \times 49 \times 96$	0.07	0.25	0.32	0.72	$\cdots$
K2	2.0	4.0	25	$25 \times 49 \times 96$	0.07	0.25	0.32	0.72	$\cdots$
K3	2.0	4.0	22	$25 \times 49 \times 96$	0.09	0.20	0.17	1.28	$\cdots$
K4	2.0	6.0	17	$25 \times 49 \times 96$	0.08	0.18	0.13	1.68	$\cdots$
K5	2.0	7.0	16	$25 \times 49 \times 96$	0.03	0.10	0.05	0.50	$\cdots$
K6	2.0	8.0	14	$25 \times 49 \times 96$	0.02	0.08	0.03	0.53	$\cdots$
AC, AC1, AC2	1.760	1.7	25	$37 \times 73 \times 144$	0.05	0.17	0.21	0.48	$\cdots$
BC, BC1, BC2	1.806	1.7	25	$37 \times 73 \times 144$	0.05	0.17	0.21	0.48	$\cdots$
CC, CC1, CC2, CC3	1.812	1.7	25	$37 \times 73 \times 144$	0.05	0.17	0.21	0.48	$\cdots$
AF, AF1, AF2	1.760	1.3	500	$25 \times 49 \times 280$	0.06	0.25	0.22	0.95	5.2
AFc	1.760	1.3	1000	$17 \times 33 \times 180$	0.09	0.37	0.33	1.43	7.8
AFf	1.760	1.3	1000	$37 \times 73 \times 420$	0.04	0.17	0.15	0.62	3.4
BF, BF1, BF2	1.806	1.3	1000	$25 \times 49 \times 280$	0.06	0.25	0.22	0.95	5.2
CF, CF1, CF2, CF3	1.812	1.3	1000	$25 \times 49 \times 280$	0.06	0.22	0.22	1.01	5.2

are global, their growth rates and pattern speeds do not depend on a radius.

We use the parameter $y_1(m)$ to obtain the value of a corotation radius $r_{\rm cr}$ for a given mode: Using the mode pattern speed

$$\Omega_p = \Omega_{\rm orb}\left(1 + \frac{y_1(m)}{m}\right)$$

and the radial profile $\Omega = \Omega(r)$ of a fluid angular velocity in the disk, we can calculate $r_{\rm cr}$ from the equation $\Omega(r = r_{\rm cr}) = \Omega_p$.

In those simulations where the disk is oscillating radially, the values of the mode amplitude D_m at a given radius oscillate due to disk oscillations, which makes it more difficult to extract the mode growth rates from D_m. In such cases, we have found that more accurate growth rates can be obtained if we use normalized root mean squared (rms) mode amplitudes G_m, defined as:

$$G_m = \langle D_m \rangle_2 / \langle D_0 \rangle_2,$$

where the angle brackets $\langle \ldots \rangle_2$ denote an rms value over radii from r_- to r_+:

$$\langle D_m \rangle_2 \equiv \frac{1}{r_+ - r_-}\left(\int_{r_-}^{r_+} |D_m|^2 dr\right)^{1/2}$$

IV. TIME EVOLUTION

In this section, we present the results of the fully general-relativistic time evolution of the initial data for reference model A, constructed as described above in Sec. III. Overall, the dynamics of model B is qualitatively similar to that of A, while model C exhibits a qualitatively different time evolution. The BH initial mass in all of our models is $2.5\mathcal{M}_\odot$, as in some of the previous works [66,72,158], and the disk rotational period $t_c = 3.667$ ms is used as a unit of time in all of the plots in this section.

At the beginning of time evolution, the metric blending procedure (described earlier in Sec. III A) introduces axisymmetric constraint-violating perturbation to the spacetime near the BH, causing an unphysical oscillation in the BH mass, which damps out in about one orbital period of the disk. We discard the first orbital period when analyzing simulation data and drawing physical conclusions about the system dynamics.

In the meanwhile, the axisymmetric perturbation propagates outwards and triggers axisymmetric disk oscillations. Disk oscillations lead to formation of shock waves, which transform kinetic energy of the shock to thermal energy, resulting in damping of the oscillations, as well as short episodes of accretion. We discuss different aspects of the dynamics of the disk in more detail below.

After about three orbital periods, the disk develops an $m = 1$ nonaxisymmetric mode, which we have identified as PP type instability [61,62] (discussed in more detail below in Sec. V). The same type of mode develops in model B, while the more slender model C develops an $m = 2$ mode of an intermediate type (see Sec. V C). As the $m = 1$ mode grows, the center of mass of the disk drifts away from its initial position along a spiral-like trajectory, as shown in Fig. 5 (red squares). As a result of gravitational interaction between the deformed disk and the BH, the latter also starts spiraling away, mirroring the motion of the disk center of mass, as shown in Fig. 5 (black line). This plot also shows dashed lines that connect the positions of the center of mass of the BH and the disk at different moments of time. As we can see, all of these lines intersect with each other at one point at the initial location of the center of mass of the disk-BH system, implying that the center of mass of the system does not move, as should be the case for BH motion caused by physical interaction with the disk (but not gauge effects).

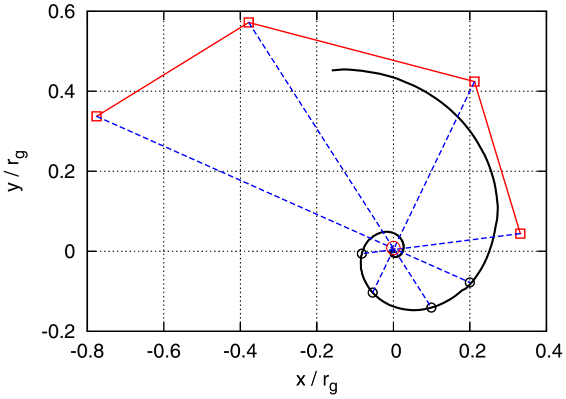

FIG. 5 (color online). Trajectories of the center of mass of the accretion disk (red line) and the BH (black line). Dashed lines show four consecutive simultaneous locations of the two centers of mass, and a small red circle at the origin marks the location of their common center of mass. The spiral motion of the BH is caused by the development of the nonaxisymmetric $m = 1$ mode in the disk.

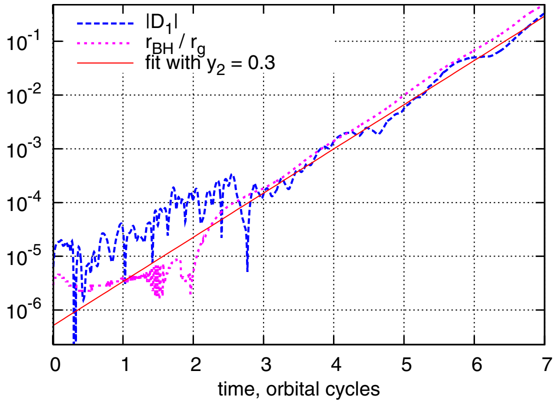

FIG. 6 (color online). Time evolution of the amplitude $|D_1|$ of the nonaxisymmetric $m = 1$ mode in the disk and the length of the BH position vector $r_{\rm BH}/r_g$. The growth of these quantities is correlated; i.e. they develop at the same time and with the same rate.

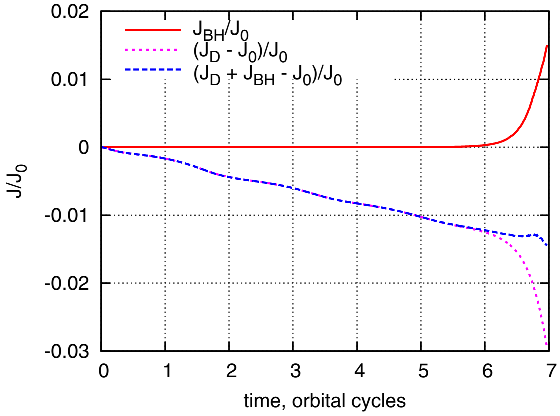

FIG. 7 (color online). Illustration of the angular momentum transfer from the disk to the BH. The solid (red) line shows the orbital angular momentum of the BH J_{BH}, the dotted (magenta) line shows the decrease in the angular momentum of the disk $J_D - J_0$, and the dashed (blue) line shows the total decrease of the angular momentum of disk + BH $(J_D + J_{\mathrm{BH}}) - J_0$. All quantities are divided by the initial value of angular momentum of the disk J_0. The noticeable angular momentum transfer can only be seen in the last orbital period, when the $m = 1$ distortion reaches significant amplitude. The gradual decrease in total angular momentum is due to the mass loss at the interpolation boundaries. This is a numerical artifact which converges away with resolution.

Figure 6 shows the time evolution of the amplitude $|D_1|$ of the $m = 1$ PP nonaxisymmetric mode and the distance r_{BH} (normalized to r_g) from the BH center to its initial position. As we can see, both $|D_1|$ and r_{BH} have the same growth rate. This feature provides another evidence that the BH motion is a result of the physical interaction with the $m = 1$ disk deformation but not due to gauge effects.

We point out that, as a result of the interaction of the $m = 1$ deformed disk with the BH, the latter acquires significant orbital angular momentum from the disk. Figure 7 illustrates how angular momentum of the disk (J_D), BH (J_{BH}),[4] and BH + disk system $(J_{\mathrm{BH}} + J_D)$ changes with time with respect to initial disk angular momentum (J_0). The total angular momentum of the disk + BH system decreases by ~1.5% in ~7 orbital periods due to numerical errors such as interpolation at the block boundaries and evaporation to the artificial atmosphere in the case of medium resolution. As a result of angular momentum transfer, J_D/J_0 additionally decreases by ~1.5%, which is completely compensated by the ~1.5% increase of J_{BH}/J_0.

Unfortunately, the continued outspiraling motion of the BH ultimately leads to the intersection of the apparent horizon with the excision boundary. At this point, the inner excision boundary conditions become ill-posed, and we have to terminate our simulations.

Similarly to the findings of [20,76], we did not observe runaway instability in all three models. This is perhaps not surprising, because the inner boundary of the disk is located at a considerable distance from the cusp in equipotential surfaces for all three models that we study. Short periodic episodes of mass transfer in models A and B caused by strong nonlinear oscillations do not lead to significant advancement of the cusp towards the disk. Moreover, the damping of radial disk oscillations in models A and B reduces and eventually completely terminates this mass transfer from the disk to the BH, preventing onset of runaway instability. Therefore, we do not expect this instability to occur at a later time. In the most likely scenario of the subsequent evolution, the development of nonaxisymmetric instabilities will redistribute disk angular momentum and lead to a profile of specific angular momentum that increases outwards [86,91].

To determine how much our results depend on numerical resolution, we have performed simulations of this model for three different resolutions with grid cell size scaling as 1:1.5:1.5^2. We refer to these as the coarse, medium, and fine resolutions, respectively, hereafter. The curvilinear geometry of the blocks was chosen to be the same for all of the three resolutions. We list the parameters of the resulting coarse, medium, and fine (denoted as AFc, AF, and AFf, respectively) grid models in Table II.

Figure 8(a) shows the L_1 and L_∞ norms of Hamiltonian constraint violation for the coarse, medium, and fine resolution simulations. This plot shows that there are two distinct regimes in the evolution of the constraints: an initial exponential decrease and a subsequent steady plateau. The latter is due to the constraint damping mechanism of our evolution scheme, in which the rate of production of discretization errors is balanced by the rate of constraint damping. Since the discretization error depends on grid cell size, the value of the plateau decreases with increasing resolution. In the case with the highest resolution, the "plateau regime" is not reached during the time span of the simulation. Figure 8(a) also shows that there is a small region of a rapid growth of the constraints at the very end of the simulations. This increase is caused by the approach of the BH apparent horizon too close to the inner excision boundary as a result of the interaction of the BH with the $m = 1$ deformation of the disk described above.

Figure 8(b) shows the time evolution of the BH mass.[5] Because the constraint violations due to the metric blending are introduced at the continuum limit, the BH mass shows an unphysical oscillation that does not converge away with resolution but which completely damps out in

---

[4] We calculate the total angular momentum of the disk using the expression $J_D = \int d^3x\sqrt{-g}T^t_\varphi$ [159], while the orbital angular momentum of the BH is calculated using a simple Newtonian estimate: Using the BH speed $r\dot{\varphi}$ and its distance from the origin r, we get $J_{\mathrm{BH}} \simeq M_{\mathrm{BH}} r^2 \dot{\varphi}$.

[5] We measure irreducible BH mass M_{BH} using the area of apparent horizon [160].

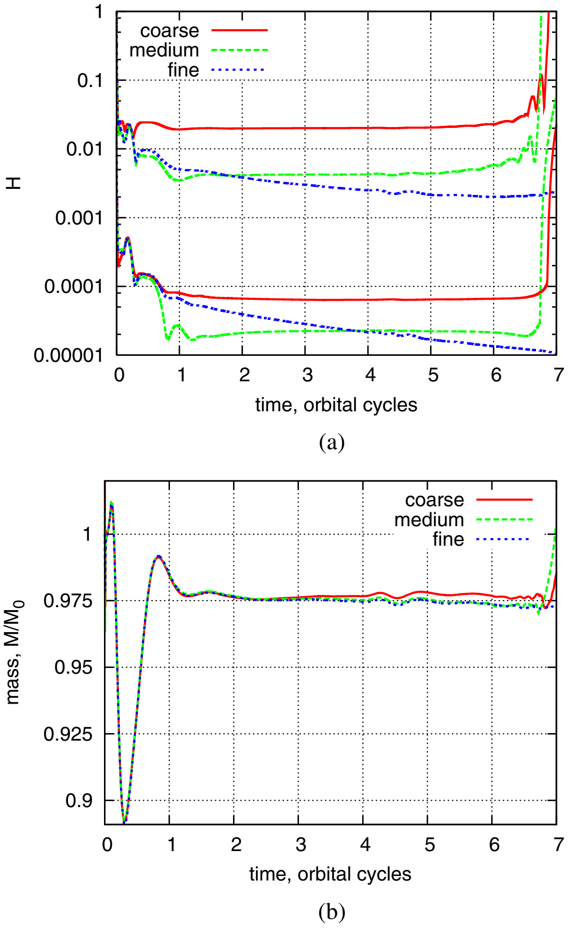

FIG. 8 (color online). Time evolution of the constraints and the BH mass for simulations with the coarse, medium, and fine resolution grids. (a) L_∞ and L_1 norms of the Hamiltonian constraints as a function of time. For the coarse and medium resolution cases, the plot shows that the constraints are reduced down to the discretization error level during the first orbital period (see the main text for more detailed discussion). (b) Time evolution of the BH mass (measured from the area of apparent horizon, normalized by its initial value). After the initial transitional oscillatory phase, the BH mass settles down to $(97.5 \pm 0.5)\%$ of its initial value. The oscillation in the first orbital period is caused by the constraint violations due to blending procedure in the construction of our initial data (see Sec. III A).

about one orbital period. The BH mass then stabilizes at $(97.5 \pm 0.5)\%$ of its initial value and remains near this value until the end of the simulation. The glitch in the BH mass by the very end of the simulation is caused by the growth of constraint violations due to the approach of the BH to the inner excision boundary as a result of outspiraling motion.

Figure 9(b) shows the relative differences in the maximum rest-mass density of the disk $\rho_{\max}$ between the coarse and medium resolutions (thick red line), as well as medium and fine resolutions (thin black line). The latter quantity is scaled by a factor of 1.5. As can be seen from the plot, the two curves agree up to ≈ 4.5 orbital cycles, which implies that the convergence is of first order during that period. This order of convergence for hydrodynamical quantities such as $\rho_{\max}$ is expected, both because of the presence of shocks in our simulations and because the hydrodynamical method that we use is only first-order convergent at local extrema of the density (see, e.g., Chap. 13 of [161]). At $t > 4.5t_{\rm orb}$ the two curves start diverging. Such behavior is due to the development of nonaxisymmetric instabilities, which are seeded by numerical errors and start to grow at different times for different resolutions.

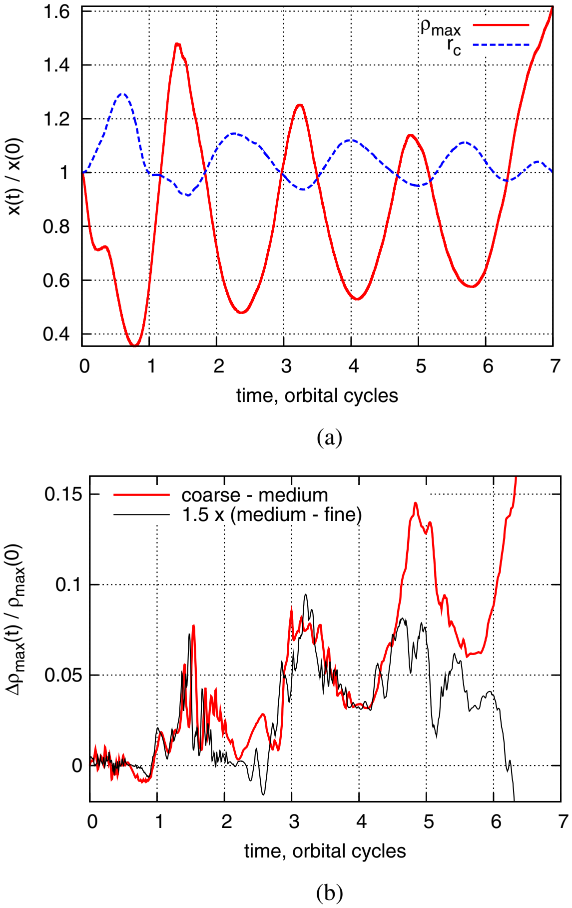

FIG. 9 (color online). Top: Time evolution of the maximum rest-mass density $\rho_{\max}(t)$ and the location of a rest-mass density maximum $r_c = r(\rho_{\max})$. Bottom: Relative differences of $\rho_{\max}(t)$ between the coarse and medium resolutions (thick red line) and between the medium and fine ones (thin black line), scaled to the first-order convergence.

The parameters y_1 and y_2 that characterize nonaxisymmetric modes (introduced in Sec. III D and discussed in more detail below in Sec. V) for medium and fine resolution models agree up to the measurement accuracy.[6] Specifically, the values of y_1 and y_2 for simulation AF are $-0.17(5)$ and $0.300(8)$, respectively, while for the

---

[6] The error in measurement of these parameters stems from the uncertainty in determining the time segment where the instability exhibits clear exponential growth.

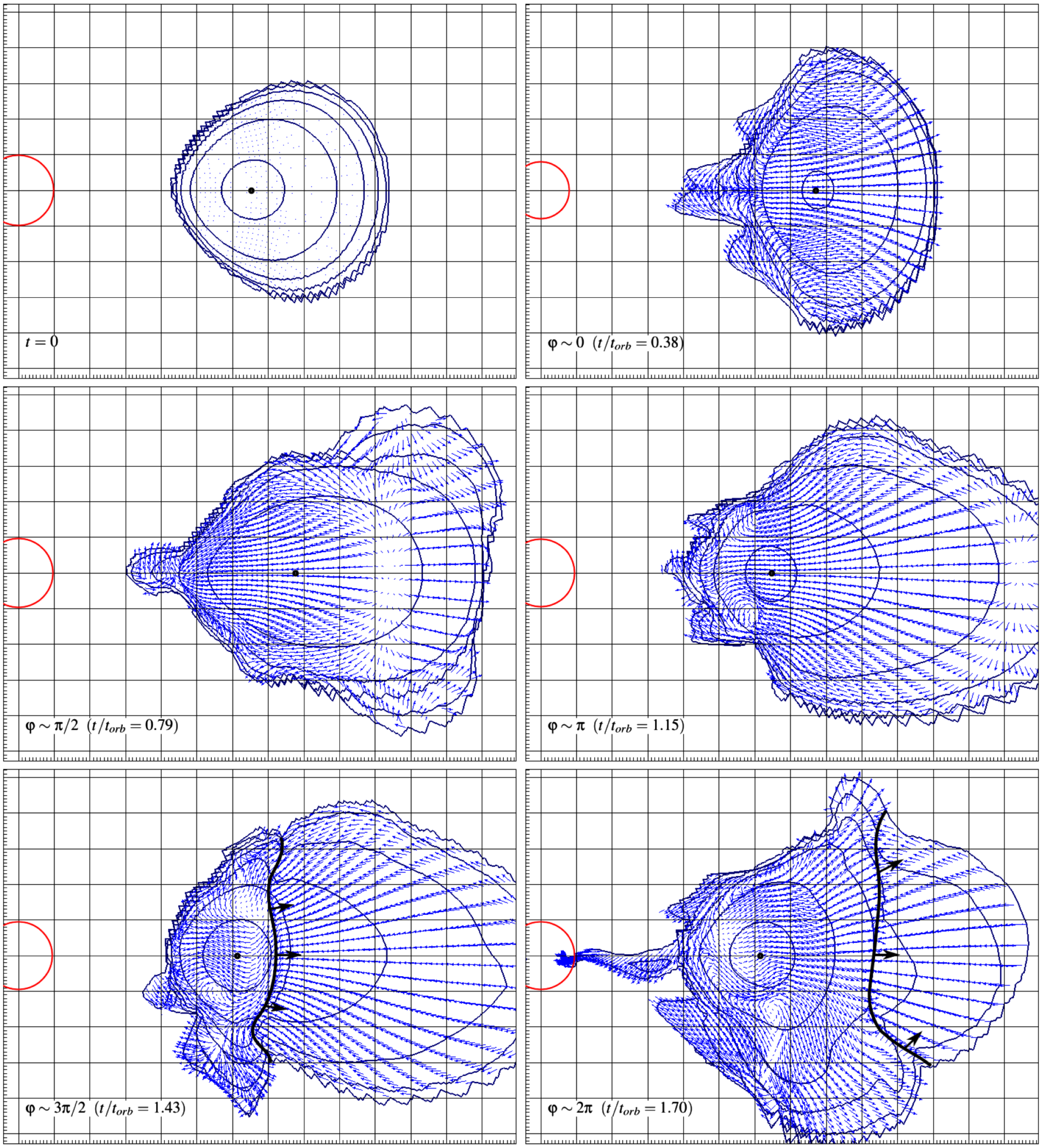

FIG. 10 (color online). Meridional cuts of the disk and the BH horizon in the xz plane at several different phases $\varphi \in (0 - 2\pi)$ of the radial oscillation. Each frame shows six density contours, equally spaced in the logarithmic scale between the initial maximum density $\rho_{\max}(0)$ and $10^{-6}\rho_{\max}(0)$. Also shown are the velocity field in the meridional plane and the location of the density maximum. The bottom two frames also show the position of the shock wave that is propagating outwards (thick black line). The last frame shows a brief episode of accretion.

simulation AFf they are $-0.17(3)$ and $0.30(1)$, respectively. The values for the coarse resolution simulation AFc [$y_1 = -0.13(5)$ and $y_2 = 0.33(1)$] depart from the values in higher resolution simulations by a small amount.

We now proceed to the analysis of the axisymmetric disk oscillations induced by the metric blending procedure (described in Sec. III A). Figure 9 shows the time evolution of the maximum disk density $\rho_{\max}$ (solid line) and the radial position of the disk center r_c[7] (dashed line), normalized to their values at $t = 0$. As can be seen from this plot, the evolution of both $\rho_{\max}$ and r_c is dominated by a single

---

[7] We define the radius of the disk center r_c to be the radius, where the φ-averaged disk density reaches its maximum.

mode of oscillation. The disk expands while moving away from the BH and contracts while moving towards the BH. This can also be seen in Fig. 10, which shows meridional cuts of the disk in the xz plane in different phases of the oscillation.

The radial oscillation of the disk has a frequency of $\sim$164 Hz, a value that is slightly smaller than the epicyclic frequency $\kappa = 201$ Hz at $r = r_c$ for a Schwarzschild BH of the same mass.[8] Rezzolla, Yoshida, and Zanotti [163] studied relativistic axisymmetric oscillations of accretion disks in the Cowling approximation using disk models that have the same Γ $(= 4/3)$ and (constant) specific angular momentum profile as the ones studied here. They found that the disks with $r_c = 3.860 r_g$ have the radial oscillation frequency of $\simeq 261$ Hz ($= 0.020\,17$ for their c2 model in normalized units [163]), which is higher than the $\sim$164 Hz frequency that we obtain in our case. Part of this difference stems from the difference in the disk models: While the model of [163] has $r_c = 3.860 r_g$, our disk model A has $r_c = 6.51 r_g$ (cf. Table I). Rezzolla, Yoshida, and Zanotti [163] have found that the oscillation frequency f depends on the disk extent L in a particular way. Namely, f decreases with increasing L, and in the limit of very thin disks ($L \longrightarrow 0$), f approaches the local value of the epicyclic frequency κ (see Fig. 4 of [163]). If we assume this dependence $f(L)$ to hold for any r_c, we can obtain the value of radial oscillation frequency for a disk with the same L and r_c as our model. This frequency turns out to be $\sim$168 Hz, which is very close to $f = 164$ Hz that we obtain in our simulations. This result might indicate that for the disks that are similar to the ones considered here, the disk self-gravity does not significantly affect the frequencies of the radial oscillations. Note that in the case of NSs, the frequency of the fundamental quasiradial modes was found to differ by a factor of $\sim$2 between the Cowling and full GR simulations [146,164], perhaps implying that the self-gravity plays a more important role in the case of NSs. However, since it is unclear whether such dependence of f on L holds exactly for other values of r_c, this result should be taken with caution. We will revisit this issue in a future publication.

The disk oscillations are damped due to formation of shock waves that convert the kinetic energy of the oscillations into the thermal one. At the end of the contraction phase of the disk, the high-density inner part of the disk bounces back earlier than the lower-density outer part. The collision of the former with the still-infalling lower-density outer material leads to formation of an outward-propagating shock wave (see the two bottom panels in Fig. 10). The shock accelerates during propagation and reached relativistic velocities of $\sim 0.3c$ in the rarefied outer disk shells. In order to quantify the amount of the shock dissipation, we evolve this model also with the isentropic polytropic EOS with the same $\Gamma = 4/3$ (in addition to the evolution with the nonisentropic Γ-law EOS), which does not allow entropy changes and thus shock heating. In this case, the oscillations exhibit little damping, while in the case of evolutions with the Γ-law EOS, the amplitude of $\rho_{\max}$ decreases by a factor of $\sim$2 in $\sim$4 orbital periods. Since the relative differences in $\rho_{\max}$ for different resolutions converge away [as illustrated by Fig. 9(b)], the oscillation damping is independent from resolution and as such cannot be caused by numerical errors. Note that dissipation of oscillation kinetic energy into heat by shocks has been found to operate in many other astrophysical scenarios, including damping of NS oscillations in a migration from an unstable to a stable branch [165,166] and in phase-transition-induced collapse of NSs [167], as well as damping of ring-down oscillations of nascent proto-NSs formed in core-collapse supernovae (e.g., [168]) and accretion-induced collapse of white dwarfs (e.g., [169]).

V. NONAXISYMMETRIC INSTABILITIES

In this section, we discuss nonaxisymmetric instabilities in the disks. First, we test our method by reproducing results obtained by Kojima [80] for thick tori with negligible self-gravity on a Schwarzschild background. In the next two sections we analyze the nonaxisymmetric instabilities in our models first on a fixed background and then with a fully dynamical general-relativistic treatment.

In various astrophysical scenarios, the disk might be formed with different nonaxisymmetric structures, leading to preferential excitation of specific unstable nonaxisymmetric modes. In order to account for these possible scenarios, in our work we evolve initial disk models with added small nonaxisymmetric perturbations at $t = 0$.

We expect [63,64,84] our thick disk models A and B to be dominated by nonaxisymmetric unstable modes with azimuthal numbers $m = 1$ and $m = 2$, while for the more slender model C instabilities with $m = 3$ and $m = 4$ should also play an important role. In our simulations without initial perturbations, these modes are triggered by numerical errors and start to grow at a random moment in time. In order to explore the evolutionary scenario in which a particular mode is excited initially, we add a small density perturbation of the form $\tilde{\rho} = \rho[1 + A \cos m(\varphi - \varphi_0)]$ to our initial disk models. We use a perturbation amplitude $A = 0.001$, which we have found to be both large enough to trigger the instability and sufficiently small to remain in the linear regime. The amount of constraint violations due to these artificial perturbations, which is quickly suppressed by our constraint damping scheme, is too small to significantly affect the subsequent evolution of the disk.

For each initial disk model A, B, and C we have completed a sequence of evolutions both in the Cowling and in

---

[8] The relativistic epicyclic frequency for the Schwarzschild metric is given by $\kappa = \frac{1}{2\pi}\sqrt{(GM/r^3)[1 - (3r_g/r)]}$ [162].

the full GR treatment. As explained in the end of Sec. III C, corresponding simulations are referred to by two- or three-letter notation (such as AC, AC1, AC2, AF, etc.), in which the first letter denotes the initial disk model (A, B, or C), the second letter is either C for the Cowling or F for the full GR treatment, and the third one is the azimuthal number m of the initial perturbation (absent if evolved without initial perturbation).

A. Comparison with previous work

Below, we present the growth rates of PP instability in evolutions of equilibrium tori in the Cowling approximation and compare them to the results obtained by Kojima [80], who studied PP instability in thick disks around Schwarzschild BHs using a linear perturbative approach. Kojima analyzed tori with constant distribution of specific angular momentum, constructed in a relativistic framework using the Abramowicz-Jaroszynski-Sikora prescription [81]. Kojima calculated the $m = 1$ mode growth parameter y_2 for several sequences of disk models with different values of specific angular momentum ℓ ($= 3.8$, 4.0, 4.2). In particular, [80] found that, due to relativistic redshift effects, y_2 for GR models is generally smaller than in the Newtonian case [63].

TABLE III. Physical parameters of the initial disk models, used for comparison with calculations by Kojima [80]. Here, r_c/r_g is the location of the density maximum in units of the BH gravitational radius r_g, r_- (r_+) is the inner (outer) radius of the torus, and $\rho_{\max}$ is the maximum density. For all models, the mass of the BH is $\mathcal{M}_\odot$, and specific angular momentum has constant value $\ell = 4.0$ and polytropic constant $K = 0.06$ (the latter two quantities are given in the normalized system of units, in which $G = c = \mathcal{M}_\odot = 1$).

Model	r_c/r_g	r_-/r_c	r_+/r_-	$\rho_{\max}$
K1	5.236	0.60	3.952	1.715×10^{-4}
K2	5.236	0.65	2.956	5.321×10^{-5}
K3	5.236	0.70	2.351	1.472×10^{-5}
K4	5.236	0.75	1.939	3.522×10^{-6}
K5	5.236	0.80	1.640	5.809×10^{-7}
K6	5.236	0.85	1.419	8.682×10^{-8}

TABLE IV. Parameters of the $m = 1$ PP instability, measured for the dynamical evolutions of Kojima disk models K1–K6. y_1 and y_2 are the pattern speed and growth rate parameters, respectively, Ω_p is the mode pattern speed, and $r_{\rm cr}$ is the mode corotation radius.

Model	y_1	y_2	Ω_p/Ω_c	$r_{\rm cr}/r_c$	Type
K1	−0.174	0.097(6)	0.826	1.136	PP
K2	−0.147	0.124(3)	0.853	1.112	PP
K3	−0.113	0.153(3)	0.887	1.083	PP
K4	−0.084	0.145(4)	0.916	1.041	PP
K5	−0.048	0.120(3)	0.952	1.060	PP
K6	−0.011	0.093(5)	0.989	1.007	PP

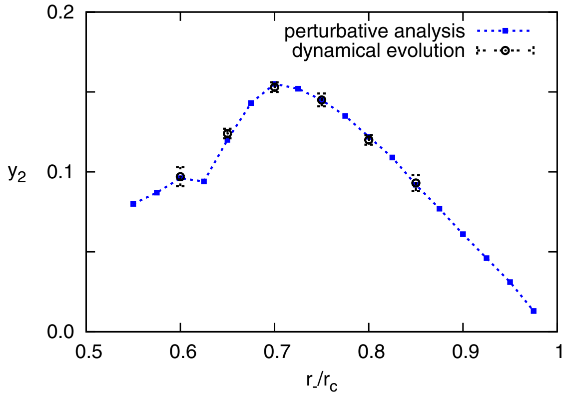

FIG. 11 (color online). Comparison of the $m = 1$ PP-mode growth rates y_2 obtained by Kojima [80] in the linear perturbative approach with the values measured from the evolutions of the same initial data models in the Cowling approximation. The abscissa represents the ratio of the inner radius of the disk r_- to the radius of the maximum disk density r_c. Note that the error bars of the measured growth rates originate from the uncertainty in determining the time span of a clear exponential growth of the mode.

We have constructed a sequence of Abramowicz-Jaroszynski-Sikora tori of varying radial extent with the same physical parameters as in [80]. All these models have polytropic index Γ of $4/3$ and specific angular momentum ℓ of 4.0. The mass of the BH is set to $M_{\rm BH} = 1$. The models in this sequence are labeled as K1–K6, and their parameters are listed in Tables III and IV. To excite the $m = 1$ mode, we add a small nonaxisymmetric perturbation as described above and evolve the disk in the Cowling approximation, using a curvilinear grid (as described in Sec. III C), adapted to each of the models. Parameters of the curvilinear grids for each model are listed in Table II. We then measure the growth rate y_2 as described in Sec. III D above and compare it with the results of Kojima.

Figure 11 shows the values of y_2 as a function of the disk radial extent for our models and for those of Kojima. As we can see, y_2 for our models are within estimated error bars from the values, calculated by Kojima in [80], as it should be the case.

B. Fixed background

In this section, we analyze nonaxisymmetric instabilities which develop when our initial disk models are evolved in the Cowling approximation. We find that all of our models develop the PP instability. More specifically, for models A and B the fastest growing mode is $m = 2$, while for the more slender model C it is $m = 3$. This is expected from the Newtonian considerations [63,64,84]. Below, we first describe instabilities in models A and B, after which we focus on model C. As mentioned above, we evolve our models with and without artificial density perturbations. For models A and B, we add $m = 1, 2$ and for model C we add $m = 1, 2, 3$ perturbations. Notice that all simulations contain a spurious $m = 4$ perturbation which is a numerical artifact of interpolation at the boundaries between four blocks near the equatorial plane. The evolutions without artificial perturbation are therefore similar to the ones in which an $m = 4$ density perturbation is added.

To analyze the nonaxisymmetric modes, we adopt an approach from Woodward, Tohline, and Hachisu [64]. Namely, we expand the disk density in the equatorial plane in a Fourier series, as explained in Sec. III D above. Then we construct and analyze the following *four diagrams*:

(i) The $D_m - t$ diagram shows a logarithm of the normalized mode amplitude D_m as a function of time at some radial location close to the disk density maximum r_c. The slope of this curve yields the growth rate y_2.

(ii) The $D_m - r$ diagram represents a radial profile of the normalized mode amplitude D_m. This diagram will be helpful in identifying the type of nonaxisymmetric instabilities [64].

(iii) The $\varphi_m - t$ diagram displays a phase angle of the nonaxisymmetric mode m as a function of time at a specified radius. The slope of this function determines the mode pattern speed and parameter y_1 that is related to it.

(iv) The $\varphi_m - r$ diagram represents the mode phase angle as a function of radius. This diagram also provides a convenient way to identify the type of the mode [64]. In all our $\varphi_m - r$ diagrams, the disk rotates counterclockwise.

We found that instabilities which develop during evolutions of models A and B are very similar. Therefore we present the properties of these instabilities on the example of model A, while the case of model C will be described separately.

Figure 12 shows the four mode diagrams for the case of model AC1, which represents time evolution of initial disk model A in the Cowling approximation with an added

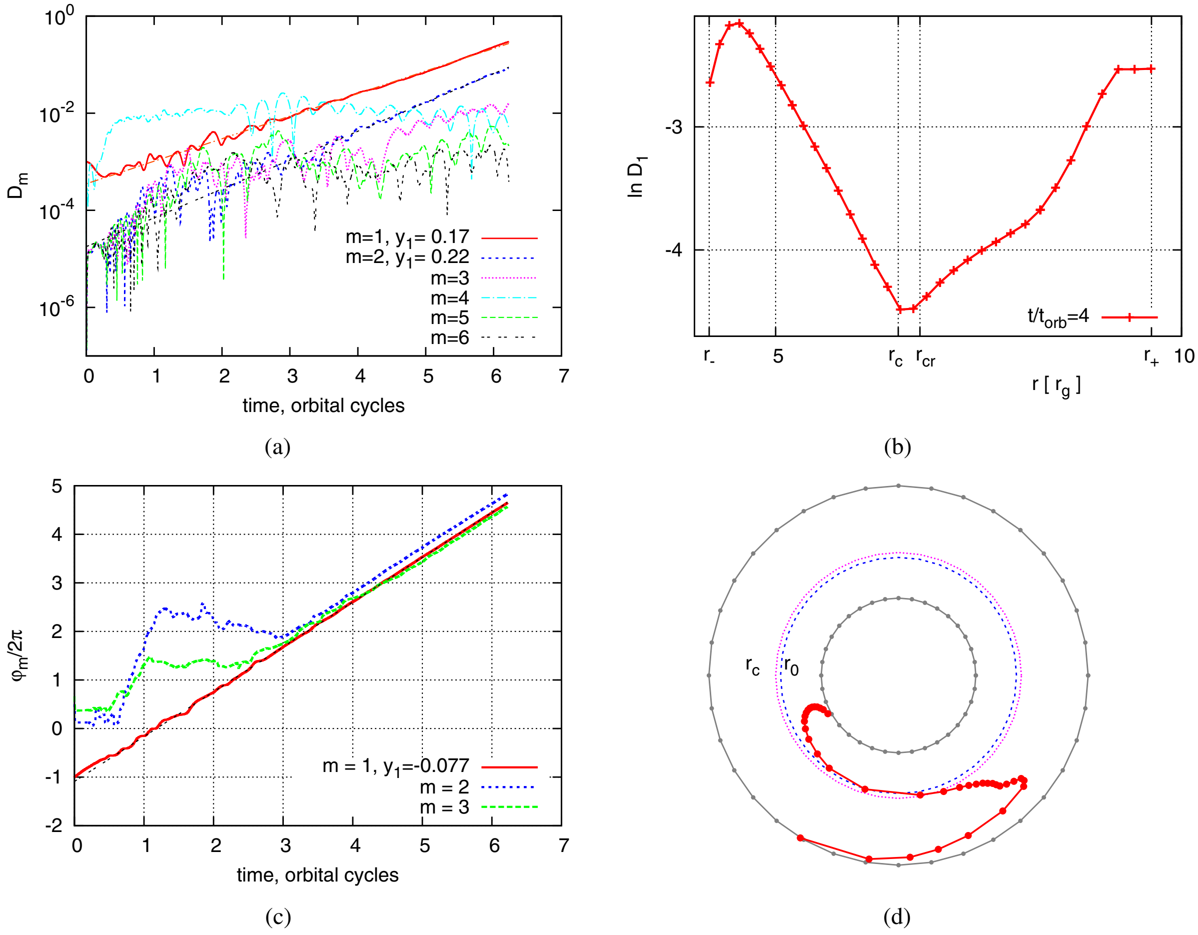

FIG. 12 (color online). The behavior of the dominant nonaxisymmetric modes and the radial character of the $m = 1$ (0, 0) PP mode in the simulation AC1: (a) The $D_m - t$ diagram shows the time evolution of the mode amplitudes D_m for $m = 1$–6; (b) the $D_m - r$ diagram shows the radial character of the $m = 1$ mode amplitude (in the logarithmic scale); (c) the $\varphi_m - t$ diagram shows the time evolution of the Fourier angle φ_m, which allows one to determine a pattern speed and a corotation radius for each mode; (d) the $\varphi_m - r$ diagram shows the dependence of the mode Fourier angle from the radius r in equatorial plane at $t/t_{\rm orb} \simeq 4$. The $D_m - r$ and $\varphi_m - r$ diagrams in (b) and (d) also show the locations of the mode corotation radius.

$m = 1$ nonaxisymmetric density perturbation. Figure 12(a) shows the $D_m - t$ diagram for the first six nonaxisymmetric modes with $m = 1, 2, \ldots, 6$. The three lowest-m modes exhibit clear exponential growth, with $m = 1$ being the dominant mode throughout the time span of the simulation (the first ≈ 6.5 orbital periods). This is the case because an $m = 1$ perturbation is artificially added from the beginning and has more time to grow and to remain the dominant mode. The mode $m = 2$ has a higher growth rate but appears subdominant, since it is triggered later than the $m = 1$ mode and has less time to develop. It may eventually overshoot the $m = 1$ mode at a later time, when both modes reach the nonlinear regime (not covered in this work; this will be a subject of our future publication). Notice that the relatively high values of the $m = 4$ mode amplitude are due to the effect of interpolation errors on four interblock boundaries of the grid near the equatorial plane.

Figures 12(b) and 12(d) demonstrate the radial structure of the $m = 1$ mode at $t = 4t_{\rm orb}$, when it is sufficiently developed. The $D_m - r$ diagram in Fig. 12(b) represents the radial profile of the amplitude of the mode. This amplitude is highest near the edges of the disk, it does not have nodes (does not become zero), and it reaches its minimum near the radius of corotation. Previous works on PP instability in Newtonian gravity [61,84] suggest that such radial behavior is a characteristic of the principal PP mode, or a mode of (0, 0) type in the classification of Blaes and Hawley [88]. The $\varphi_m - r$ diagram in Fig. 12(d) has a specific S-shaped structure, which is also a well-known feature of the PP instability, discovered in previous Newtonian works [64,84].

Finally, Fig. 12(c) shows the $\varphi_m - t$ diagram for the $m = 1$–3 modes. It shows that while all modes initially have arbitrary phases and pattern speeds, they eventually settle to the pattern speed of the dominant $m = 1$ mode possibly due to nonlinear interaction between the modes. The pattern speed of the $m = 1$ mode is slightly below the speed of the disk at r_c, which means that the mode corotation radius $r_{\rm cr}$ lies just outside r_c. The close proximity of the mode corotation radius to the radius of the disk density maximum is also typical for PP nonaxisymmetric instabilities, as discovered in previous Newtonian works [61,64,82]. All these features allow us to conclude that the observed $m = 1$ mode is indeed the PP instability.

Figure 13 shows the set of four diagrams for simulation AC2, in which an $m = 2$ density perturbation is added

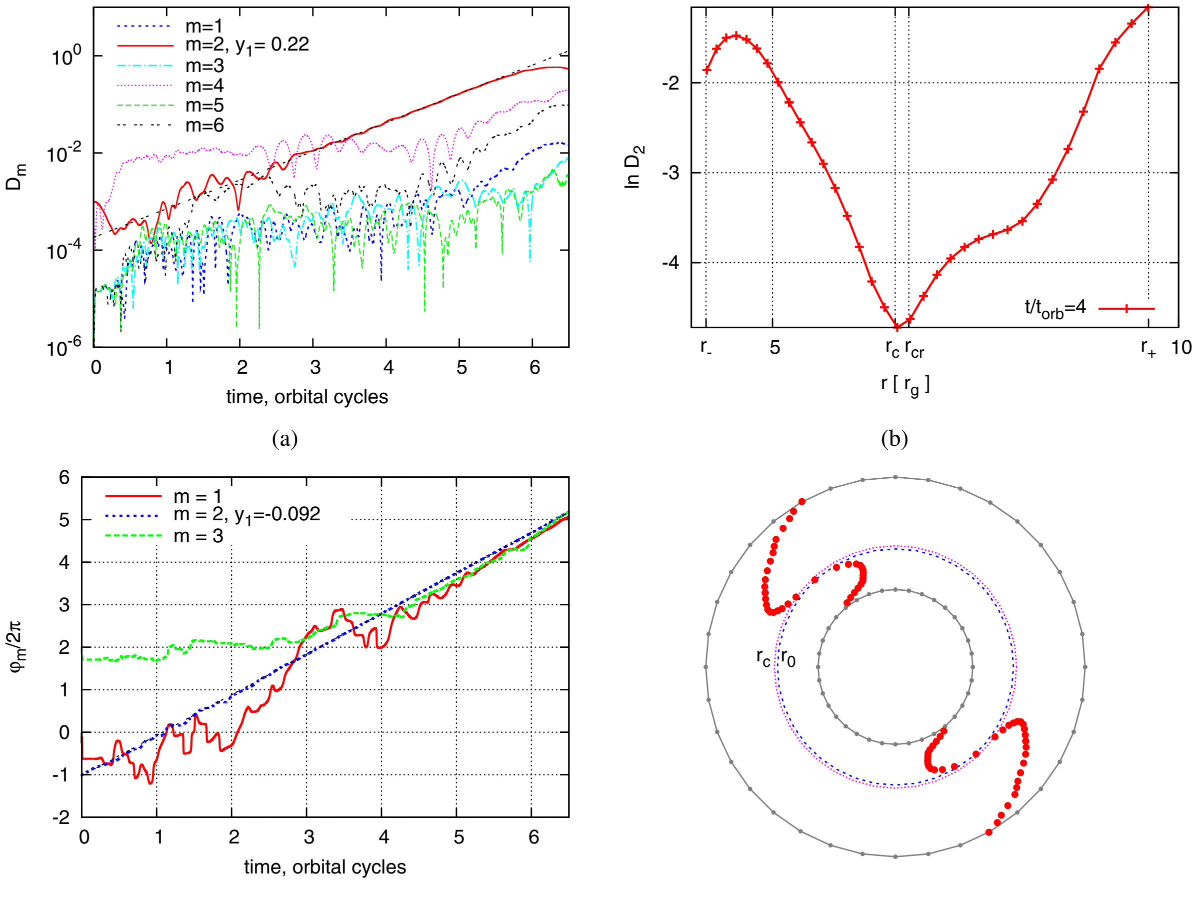

(a) (b)

(c) (d)

FIG. 13 (color online). The behavior of the dominant nonaxisymmetric modes and the radial character of the $m = 2$ (0, 0) PP mode in the simulation AC2 (see the caption of Fig. 12 for details).

TABLE V. Quantitative characteristics and types of the nonaxisymmetric modes for the simulations studied in Sec. V. For each of the simulations, the table lists one or two dominant unstable modes.

Cowling							Full GR						
Model	m	Type	y_1	y_2	Ω_p/Ω_0	$r_{\rm cr}/r_c$	Model	m	Type	y_1	y_2	Ω_p/Ω_0	$r_{\rm cr}/r_c$
AC	2	PP	−0.10(5)	0.21(1)	0.89(2)	1.07(1)	AF	1	PP	−0.17(5)	0.300(8)	0.83(5)	1.12(4)
AC1	1	PP	−0.08(4)	0.17(1)	0.93(2)	1.04(1)	AF1	1	PP	−0.18(5)	0.294(8)	0.82(5)	1.11(4)
AC2							AF2	1	PP	−0.17(3)	0.30(1)	0.83(3)	1.12(3)
	2	PP	−0.09(5)	0.22(1)	0.95(2)	1.03(1)		2	I	−0.6(1)	0.17(3)	0.68(5)	1.26(6)
BC	1	PP	−0.04(5)	0.16(1)	0.96(5)	1.03(3)	BF	1	PP	−0.16(5)	0.28(3)	0.84(5)	1.12(4)
	2	PP	−0.12(6)	0.18(1)	0.94(3)	1.04(2)							
BC1	1	PP	−0.06(5)	0.16(1)	0.94(5)	1.04(3)	BF1	1	PP	−0.12(5)	0.270(8)	0.88(5)	1.08(4)
BC2	1	PP	−0.04(5)	0.17(1)	0.96(5)	1.03(3)	BF2	1	PP	−0.13(5)	0.29(2)	0.87(5)	1.09(4)
	2	PP	−0.08(6)	0.17(1)	0.96(3)	1.03(2)		2	I	−0.5(1)	0.11(2)	0.75(5)	1.19(5)
CC	3	PP	−0.06(5)	0.21(2)	0.98(2)	1.01(1)	CF						
	4	PP	−0.04(5)	0.14(1)	0.99(2)	1.00(1)		4	I	−0.84(8)	0.16(1)	0.79(2)	1.14(2)
CC1	3	PP	−0.04(5)	0.24(1)	0.99(2)	1.00(1)	CF1	1	PP[a]?	??	??	-	-
	4	PP	−0.04(5)	0.16(2)	0.99(2)	1.00(1)		4	I	−0.84(8)	0.15(1)	0.79(2)	1.14(2)
CC2	2	PP	−0.04(5)	0.20(1)	0.99(2)	1.00(1)	CF2	2	I	−0.6(1)	0.279(7)	0.66(5)	1.26(5)
	3	PP	−0.06(5)	0.22(1)	0.98(2)	1.01(1)		4	I	−0.8(2)	0.16(1)	0.80(5)	1.14(4)
CC3	3	PP	−0.07(5)	0.23(1)	0.98(2)	1.01(1)	CF3	3	I	−0.7(1)	0.318(8)	0.76(3)	1.17(3)
	4	PP	−0.04(5)	0.15(2)	0.99(2)	1.00(1)		4	I	−0.80(8)	0.16(2)	0.80(2)	1.14(2)

[a] For the simulation CF1, it was not possible to accurately determine the growth rate and pattern speed of the $m = 1$ mode. We classified this mode as a PP type due to the character of its $\varphi_m - r$ and $D_m - r$ diagrams, which are typical for the PP modes.

initially. Figure 13(a) represents the $D_m - t$ diagram for the modes with $m = 1$–6. In this case, only the mode with $m = 2$ exhibits pronounced exponential growth. The rest of the modes either remain stable or are not excited, showing rapid growth only in the very end of the simulation, when the amplitude of the $m = 2$ mode reaches the nonlinear regime and coupling between the modes becomes important. Figures 13(b) and 13(d) show the radial profile and azimuthal shape of the mode. These are again typical for the principal $(0, 0)$ type PP instability with $m = 2$. Figure 13(c) shows the $\varphi_m - t$ diagram for the $m = 1$–3 modes. The dominant $m = 2$ mode rotates uniformly in the same direction with the disk, while the other two modes do not exhibit clear rotation pattern until after ~4 orbital periods, when they align in phase with the $m = 2$ mode. The pattern speed of the dominant mode inferred from this plot corresponds to the corotation radius just outside of r_c. Similarly to the simulation AC1 above, all these features are typical of the PP instability, studied in previous works in the Newtonian approximation [61,64,82].

While unstable modes in model B are very similar to those of model A, in model C higher-order PP modes become dominant. This is expected [63] since model C is more slender than models A and B. Indeed we observe that the most unstable mode for model C is the $m = 3$ PP mode, while $m = 2$ and $m = 4$ have comparable but smaller growth rates. The four diagrams for $m = 3, 4$ modes are not qualitatively different from those for the $m = 1, 2$ modes in simulations AC1 and AC2 above. They also exhibit all the features typical of the PP instability described above.

We can therefore conclude that the PP instability with various values of azimuthal number m is observed in all of our disk models in the Cowling approximation. For the reader's reference, the parameters of unstable modes calculated for all of our simulations are summarized in Table V.

C. Dynamical background

We now turn to the analysis of nonaxisymmetric instabilities, which develop when the disks are evolved in a fully dynamical general-relativistic framework. We again consider evolutions with and without artificial density perturbation, adding $m = 1, 2$ perturbations for models A and B and $m = 1, 2, 3$ perturbations for model C. While we observe PP-type instabilities in the Cowling case, in the fully dynamical GR case we observe two distinct types of instabilities: the PP type and a GR analog of the so-called intermediate type (I type) instability [89,91]. As in the Cowling case, instabilities in the moderately slender models A and B have very similar properties, so it suffices to present the result only for the case of model A. Model C is more slender and therefore favors instabilities with higher azimuthal numbers than those of models A and B, so we consider this model separately.

For the analysis of nonaxisymmetric modes we adopt the same approach as in Sec. V B above for simulations on a fixed background, with one exception: For evaluating mode growth rates y_2, instead of D_m, we use quantities G_m introduced in Sec. III D above. This is necessary because the values of the mode amplitudes D_m at a fixed radial location oscillate due to disk oscillations, making it hard to infer accurate growth rates of the modes. We have found that mode growth rate y_2 can be calculated more accurately from a time behavior of G_m, because it is expressed in terms of integrals over the radius and as such it is much less affected by radial oscillations. With this exception, we follow the same approach as described in Sec. V B to determine mode types, growth rates, and pattern speeds. These quantities for all models are tabulated in Table V for reference.

In most of the simulations with fully dynamical GR, the BH responds to the excitation of the $m = 1$ mode by developing an outspiraling motion, as described earlier in Sec. IV. The position vector $\bar{r}_{\rm BH}$ of the BH starts to rotate with approximately constant angular velocity $\Omega_{\rm BH}$, while the length of this vector grows exponentially. In order to characterize this motion and study it in the context of the development of nonaxisymmetric modes, we plot the time evolution of the BH position vector length $r_{\rm BH}/r_g$ and phase angle $\varphi_{\rm BH}$ on the $G_m - t$ and $\varphi_m - t$ diagrams, respectively. From these plots we can calculate the quantities $\Omega_{\rm BH}/\Omega_0$ and $y_2({\rm BH})$ that can be directly compared to those of nonaxisymmetric modes. These quantities are also listed in Table V.

Figure 14 shows the time evolution and radial profiles of the amplitudes and Fourier angles of the dominant unstable modes for the simulation AF1, which represents fully dynamical GR evolution of the initial disk model A with an added $m = 1$ density perturbation. The top left panel contains the time evolution of G_m for $m = 1$–4 and the normalized coordinate length of the BH position vector $r_{\rm BH}/r_g$. The diagram shows that the $m = 1$ mode is the dominant one. It also shows that the BH responds to the growth of the $m = 1$ mode and the distance from the BH to the origin grows exponentially at the same rate as the dominant $m = 1$ mode.

Figure 14(c) shows the time evolution of the Fourier phase angles φ_m for $m = 1, 2, 3$, measured at a fixed radial coordinate location near the inner edge of the disk r_-. The phase of the dominant $m = 1$ mode after a short initial readjustment exhibits almost uniform linear growth. Readjustment of the mode happens because the added artificial perturbation initially does not have the right shape of the mode and needs some time (less than one orbital period) to readjust itself. Similar behavior is observed in the corresponding Cowling simulation, but it is less

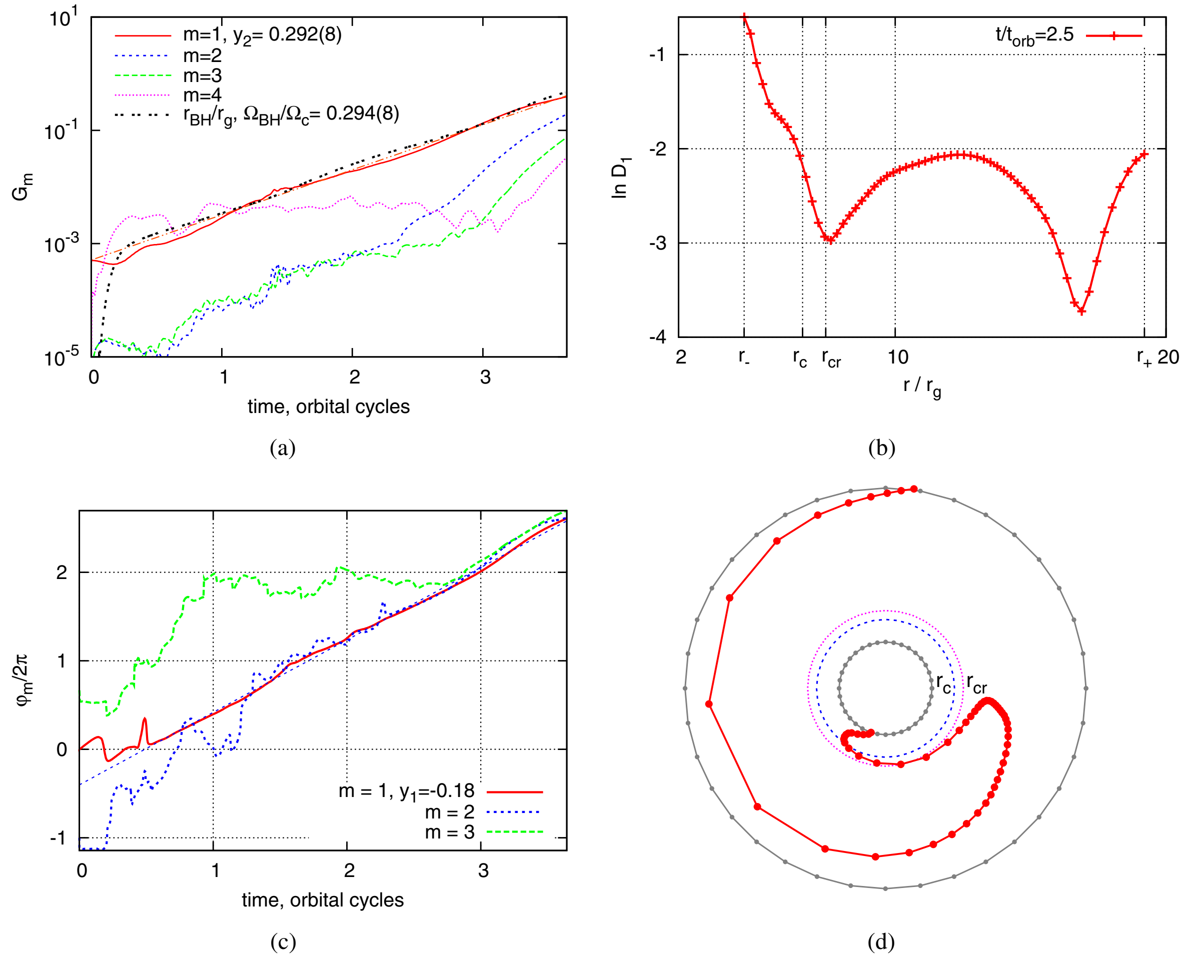

(a) (b)

(c) (d)

FIG. 14 (color online). The behavior of the dominant nonaxisymmetric modes and the radial character of the $m = 1$ (0, 0) PP mode in the simulation AF1 (see the caption of Fig. 12 for details).

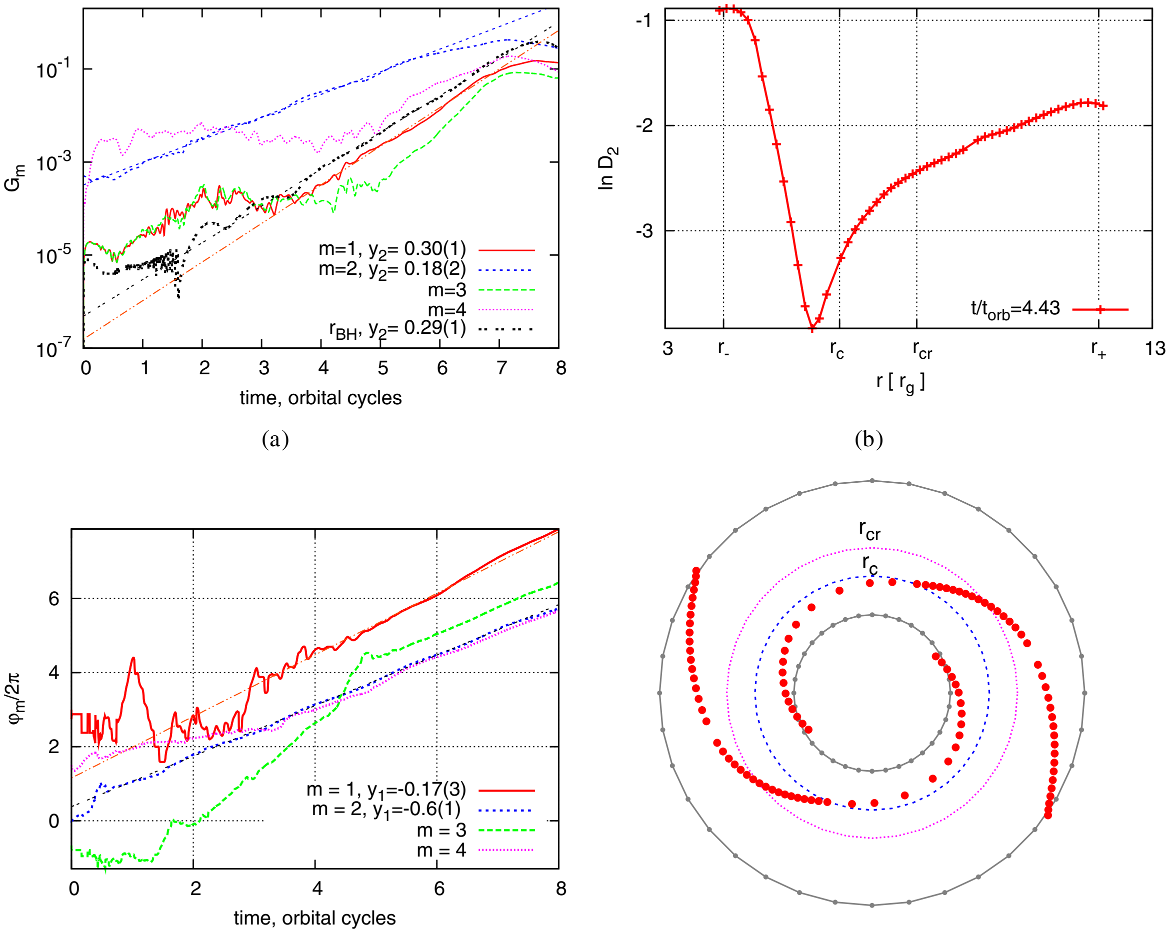

(a) (b)

(c) (d)

FIG. 15 (color online). The behavior of the dominant nonaxisymmetric modes and the radial character of the $m = 2$ I mode in the simulation AF2 (see the caption of Fig. 12 for details).

pronounced [see the $m = 1$ phase angle during the first half orbit in Fig. 12(c)]. Phases of the rest of the modes initially do not show uniform linear growth, but as the amplitude of the $m = 1$ mode increases, the higher-order modes start to align in phase with the dominant $m = 1$ mode, most likely due to nonlinear mode interaction. Notice that the pattern speed of the $m = 1$ mode calculated from this diagram is lower compared to the Cowling case.

Figures 14(b) and 14(d) show the radial and angular profiles of the dominant $m = 1$ mode at $t = 2.5t_{\mathrm{orb}}$. The location of r_-, r_+, and r_c shown in the plot refers to the same time. Because the disk undergoes radial oscillations, special care must be taken when calculating the mode corotation radius r_{cr}, which is an important quantity that characterizes nonaxisymmetric modes. To find r_{cr}, we solve an equation between the mode pattern speed Ω_p and the disk angular velocity: $\Omega(r_{\mathrm{cr}}) = \Omega_p$. The latter changes during the evolution of the disk, so strictly speaking the value of r_{cr} will also depend on time. However, we have found that in all our simulations the change of the profile of Ω in the course of the evolution is very small; therefore within the measured accuracy the corotation radius is independent of time. The values of r_{cr}/r_c, calculated in this way for all simulations on a dynamical background, are also listed in Table V. For simulation AF1, r_{cr} lies outside of r_c with $r_{\mathrm{cr}}/r_c \approx 1.17$. Such a value of r_{cr}/r_c is typical for a PP instability and comparable to the values observed in previous Newtonian studies with a moving central object and a massive self-gravitating disk [64].

Similar to the Cowling case, the radial profiles of D_m and φ_m show structural features that are typical for a PP instability of (0, 0) type in the Blaes and Hawley classification [88]. In particular, the mode amplitude displayed in Fig. 14(b) is higher near the edges of the disk and has a minimum near corotation r_{cr}. The mode amplitude does not vanish anywhere in the disk, which characterizes the mode as having type (0, 0). The profile of the Fourier angle of the mode, shown in Fig. 14(d), has a specific S-shaped

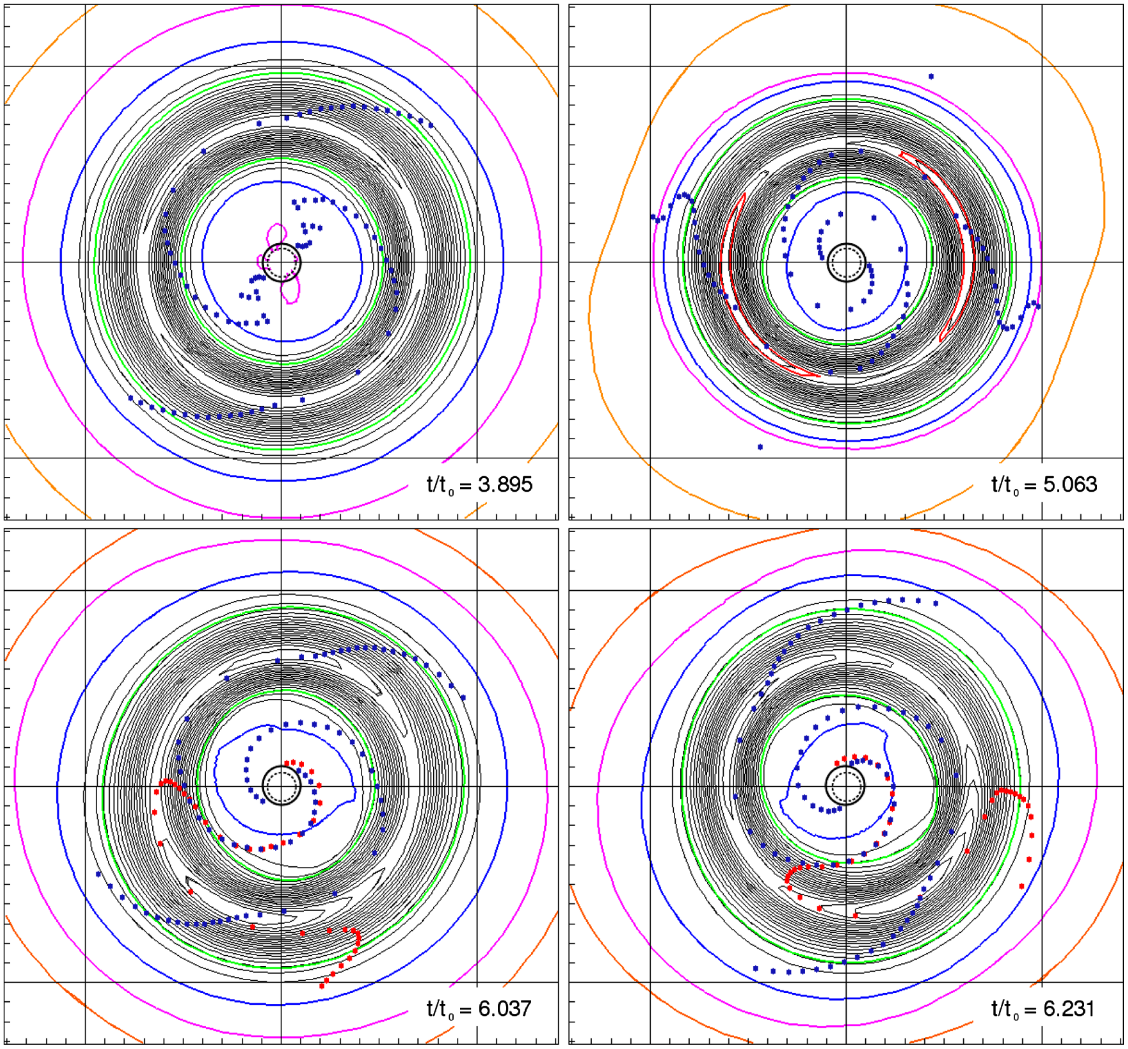

FIG. 16 (color online). A sequence of four successive snapshots of the disk density in the equatorial plane, combined with the corresponding $\varphi_m - r$ diagrams for the $m = 1$ and $m = 2$ modes for the simulation AF2. The radial character of the $m = 1$ and $m = 2$ modes is represented by a sequence of red and blue dots, respectively.

structure that consists of a trailing spiral pattern outside the corotation radius,[9] a leading spiral pattern inside the corotation radius, and a short segment near $r_{\rm cr}$ that connects the two spiral patterns.

However, compared to the Cowling approximation, the growth rate of the $m = 1$ mode is amplified by almost a factor of ~1.5, and there are reasons to believe that the outspiraling motion of the BH is responsible for this amplification. The mechanism which drives the unstable outspiraling motion of the BH is similar to the one described in [94]. The disk creates a hilltop potential, which has a maximum at the origin, so the BH initially is located at the point of unstable equilibrium. The BH can reduce its potential energy by converting it into kinetic energy of orbital motion around the common center of mass of the disk + BH system. Such orbital motion requires angular momentum which can be borrowed from the disk through the development of a nonaxisymmetric $m = 1$ mode. Because the orbital motion of the BH requires a compensating displacement of the disk center of mass, removing angular momentum from the disk increases the amplitude of the $m = 1$ mode, which in this case is the PP mode.

Next we consider the dominant nonaxisymmetric modes that develop in the simulation AF2, in which an $m = 2$ density perturbation was added. Figure 15 presents the time evolution and radial profiles of G_m and φ_m of these modes. Comparing Fig. 15 to Fig. 12, which presents the same set of diagrams for the Cowling simulation AC2, we can see that the type of the $m = 2$ mode in this simulation is quite different from the PP one observed in the simulation AC2. First, in the $D_m - r$ diagram in Fig. 15(b), the

---

[9] We remind the reader that the disk rotates counterclockwise on all $\varphi_m - r$ diagrams.

minimum of D_m lies inside r_c, unlike the case of the PP mode where such a minimum is located close to the mode corotation radius $r_{\rm cr}$. Second, the $\varphi_m - r$ diagram of the $m = 2$ mode in Fig. 15(d) consists only of trailing spirals and does not have a leading spiral pattern inside corotation, as would be the case for PP modes. Finally, as Fig. 15(d) illustrates, the mode phase angle makes an abrupt turn by $\pi/2$ radians near r_c, which would be the case when the disk were subjected to an elliptic (barlike) deformation.

Overall, this mode looks very similar to the so-called intermediate type (I type) modes found in earlier studies using Newtonian gravity (see [64,89–91]). In particular, [64] observed the I modes in their 3D Newtonian simulations of self-gravitating disks with various disk-to-central object mass ratios M_D/M_c and values of parameter $T/|W|$ (see Sec. 4 in [64]). A subset of their models that develop the I-mode instability (namely, E31 and E32) have parameters $M_D/M_c = 0.2$, $T/|W| \sim 0.47$, and $4\pi G\rho/\Omega_c \sim 4$, which are comparable to those of our models A or B (listed in Table I). Notice that in this simulation the $m = 1$ mode is also excited, as can be inferred from Fig. 15(a). The growth rate and pattern speed of this mode is the same as in simulation AF1 (cf. Table V). The $m = 1$ mode development is again correlated in time with outspiraling motion of the BH, which is apparent in Fig. 15(a). The analysis of the mode character, similar to the one performed abov, confirms that in this simulation the $m = 1$ mode has the same (0, 0) PP type as in the simulation AF1. It grows faster than the $m = 2$ mode, so that both modes become of comparable amplitude by the end of the simulation. The radial character of the two coexisting modes is also depicted in Fig. 16, which shows a sequence of snapshots of the $\varphi_m - r$ diagrams at different times, superimposed with the disk density in equatorial plane.

In the case of model C, we used artificial density perturbations with $m = 1, 2, 3$ and observed the development of four unstable modes. The same analysis that we have done before for models A and B reveals that only the $m = 1$ mode has PP type, while the modes with $m = 2, 3, 4$ have I type. The I modes with $m = 3$ and $m = 4$ represent triangular and square deformations of the disk, respectively. Such modes were previously observed in Newtonian simulations of narrow self-gravitating annuli [90]. Figure 17 shows the time behavior of G_m and

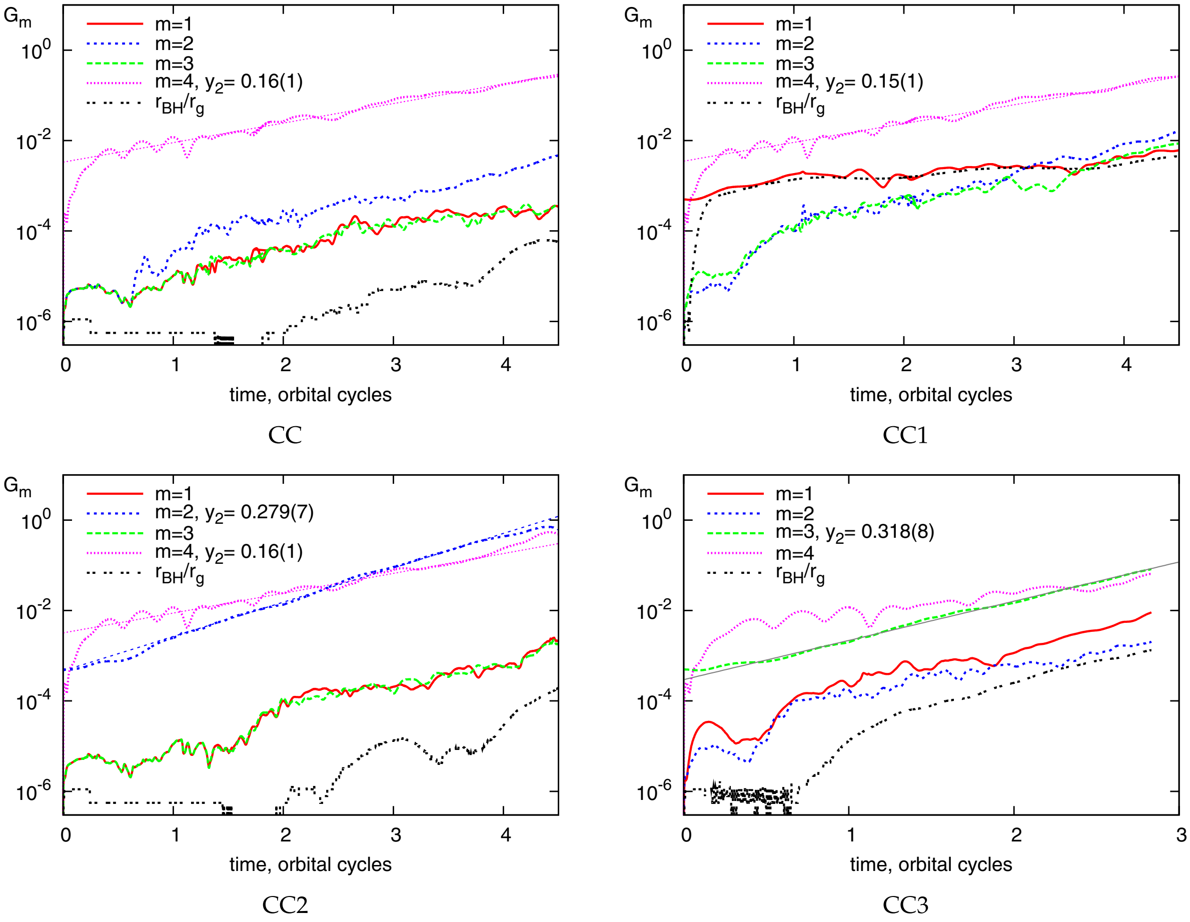

CC

CC1

CC2

CC3

FIG. 17 (color online). $G_m - t$ diagrams for modes with $m = 1$–4 in simulations with disk model C.

r_{BH}/r_g for simulations of model C with different added perturbations. As can be seen from these plots, the fastest growing mode is the I mode with $m = 3$, while the slowest one is the $m = 1$ PP mode (cf. Table V). The latter remains subdominant in all simulations, its growth does not show clear exponential behavior, and it is poorly correlated with the motion of the BH. This happens because the $m = 1$ mode does not form a global coherent pattern. In this case, the quantity G_m does not correspond to the amplitude of a global mode but rather to some combination of local $m = 1$ Fourier harmonics. However, as soon as the amplitude of the $m = 1$ mode reaches $G_m \sim 10^{-4}$, it shows a better correlation with the motion of the BH, as can be seen in Fig. 17 for simulations CC1 and CC3.

In model C, the $m = 1$ mode starts growing when the other modes with higher m have already reached significant amplitudes ($G_m \sim 0.1$). Moreover, the growth rate of the $m = 1$ mode has different values depending on which of the higher-m modes dominates the dynamics of the disk. For example, in models CF1, CF2, and CF3, in which the modes with $m = 4$, $m = 2$, and $m = 3$ reach the largest amplitudes, the $m = 1$ mode has the growth rates of 0.11, 0.23, and 0.28, respectively. Such behavior of the growth rates is likely to be a result of nonlinear interaction between these modes. In other words, the $m = 1$ mode is never linearly independent from the $m > 1$ modes, making it hard to explore unambiguously the influence of the BH motion on the growth rate of the $m = 1$ mode.

Finally, we need to point out that the comparisons with the Cowling simulations presented in this section should be taken with a grain of salt. The initial perturbation introduced by the blending of two metrics in the initial data changes the BH mass by a small amount ($\approx 2.5\%$), which not only drives the disk out of equilibrium but also changes the equilibrium configuration itself. Therefore, strictly speaking, the disks in Cowling and full GR represent different objects and cannot be directly compared. As a result, these disks will have different evolutionary paths not only due to dynamical GR effects but also due to differences in BH masses. However, because the latter is small, we believe that the differences in evolution are mainly caused by the former, while the latter should not affect the time evolution significantly. For example, for models A and B which have different disk-to-BH mass ratios (0.24 vs 0.17), we do not observe qualitative differences in time evolution, and quantitative differences are small (e.g., the differences in the growth rates are within 6%). Therefore, we conclude that most of the differences between our Cowling and full GR simulations are caused by the effects of GR.

D. Gravitational wave detectability

As mentioned before in Sec. IV, all of our disk models are unstable to nonaxisymmetric modes. Once formed, these modes start growing exponentially until they reach a saturation regime due to nonlinear effects. This process is accompanied by a redistribution of the angular momentum of the disk until the profile of the specific angular momentum becomes steep enough for the disk to be stable to nonaxisymmetric instabilities (see the related discussion in [86,91]). Before the angular momentum is redistributed, and even after the disk becomes stable, the amplitude of nonaxisymmetric modes in the disk is likely to remain high (possibly near the saturation level) [86]. The presence of nonaxisymmetric deformations in the disk leads to emission of potentially detectable gravitational radiation.

TABLE VI. Minimal number of wave cycles needed for gravitational waves from nonaxisymmetric instabilities to be detectable by LIGO, Advanced LIGO, and Einstein Telescope (ET). It is assumed that the value of the amplitude of the instability is at least $D_m = 0.1$ during this time. Estimates are given for the sources with parameters of models A and C, located at distances 10 kpc and 18 Mpc.

Source	LIGO	Adv. LIGO	ET
A at 10 kpc	1	1	1
C at 10 kpc	2	1	1
A at 18 Mpc	1.7×10^6	7900	40
C at 18 Mpc	6.4×10^6	80 000	150

Below, we give estimates of the detectability of the GW signal from saturated nonaxisymmetric instabilities in our disk models. We make our estimates based on the Newtonian quadrupole formula for the initial disk models with an added $m = 2$ mode with an amplitude $D_m = 0.1$. We calculate an approximate number of cycles that the instability needs to remain at that amplitude in order for the emitted GW to be detectable. These numbers are listed in Table VI for an event at a distance of 10 kpc (our Galaxy) and 18 Mpc (a distance to the Virgo cluster), for models A and C. The table shows that an event in our Galaxy will be detectable with the current Laser Interferometer Gravitational-Wave Observatory (LIGO) detector even with a single cycle of the nonaxisymmetric mode. An event in the Virgo cluster, on the other hand, is unlikely to be detectable with the current LIGO detector, since it would require an unrealistically large number ($> 10^6$) of cycles. Second- and third-generation detectors such as the Advanced LIGO and the Einstein Telescope can detect such events if nonaxisymmetric modes persist for $\sim 10^4$–10^5 and ~ 40–150 cycles, respectively. Finally, we point out that it is currently unclear how long a nonaxisymmetric mode in a given disk model will persist in the nonlinear regime. This is likely to depend on the details of nonlinear mode properties, accretion rate, magnetic fields and the thermodynamic state of the disk matter [86].

VI. CONCLUSION

In this paper we have explored nonaxisymmetric instabilities in self-gravitating disks around BHs using three-dimensional hydrodynamical simulations in full GR. We studied several moderately slender and slender models with disk-to-BH mass ratio ranging from 0.11 to 0.24. The parameters of these models are listed in Table I.

To obtain a self-consistent equilibrium disk model outside a BH, we solve the coupled system of Einstein constraints and Euler equations using an iterative Green functions approach, implemented in the RNS code [150]. To avoid coordinate singularities, we transform the stationary initial data outside the BH horizon from quasi-isotropic to nonsingular horizon-penetrating coordinates. We set the data inside the BH horizon to the analytic Kerr-Schild solution and smoothly blend it with the computed data outside the horizon.

We evolve the metric using a first-order form of the generalized harmonic formulation of the Einstein equations with adaptive constraint damping. The metric evolution equations are discretized on multiblock grids and solved using eighth-order finite difference operators. We evolve the matter with relativistic hydrodynamics equations in flux-conservative form, using a finite volume cell-centered discretization scheme. We use a Γ-law equation of state to model disk matter. Our numerical approach makes extensive use of the curvilinear mesh adaptation in order to achieve desired resolutions in different parts of the domain.

We did not observe the runaway instability in our models. This is perhaps not surprising because in our models the Roche surface is open and the inner edge of the disk is widely separated from the cusp in equipotential surfaces (see Fig. 3). Brief episodes of accretion that we observed do not transfer enough mass to change the configuration of the Roche lobe. Therefore, the absence of the runaway instability is mainly the consequence of the particular choice of models and does not exclude the possibility that the instability develops in models with different initial parameters, especially in models with smaller specific angular momentum.

In all models that were explored we observed unstable nonaxisymmetric modes. We have performed detailed analysis of these modes to determine their types, growth rates, radial profiles, and pattern speeds (see Table V). For all simulations in the Cowling approximation we observe the development of the PP instability with $m = 1$–4. In this case, the azimuthal number m of the fastest growing mode depends on the disk slenderness: For moderately slender models A and B such a mode is $m = 2$, while for the more slender model C, it is $m = 3$. In the simulations in full GR, we observe two distinct types of instabilities. The unstable mode with $m = 1$ has PP type, similar to the one observed in the Cowling case. Unstable modes with $m > 1$ become the intermediate modes (I modes), representing elliptical, triangular, or square deformations of the disk. In full GR, the fastest growing mode is $m = 1$ in models A and B and $m = 3$ in model C.

In the full GR case, the development of the $m = 1$ PP mode is accompanied by an outspiraling motion of the BH. The distance from the BH center to its initial position has the same growth as that of the $m = 1$ mode amplitude. We find that due to this motion, the growth rate of the $m = 1$ mode is amplified by a factor of ≈ 1.5 compared to the Cowling case for massive models A and B. This amplification makes the $m = 1$ PP mode the fastest growing one in models A and B, while in the case of the less massive model C, this mechanism is not as efficient. The overall picture of the unstable modes in full GR is qualitatively similar to and consistent with the Newtonian case [64,80,90].

Evolution of nonaxisymmetric instabilities in the nonlinear regime will be associated with the emission of high-frequency gravitational radiation. In Table VI, we give rough estimates of the detectability of this radiation in terms of the number of cycles that a nonaxisymmetric deformation must persist in order to be detectable. While even a single cycle of gravitational radiation from this deformation is detectable if it occurs in our Galaxy, for more reasonable distances such as the Virgo cluster it is only detectable with Advanced LIGO, and only in the case that the disk deformation persists for thousands of cycles (see Table VI). It is currently unclear how long a nonaxisymmetric deformation can persist in the nonlinear regime.

Finally, we would like to point out limitations of our current simulations. We use simplified initial disk models and do not include realistic microphysics, neutrino cooling, and magnetic fields. Future studies of nonaxisymmetric instabilities should take into account these effects, as well as consider a larger set of parameters, such as nonconstant angular momentum distribution, various disk sizes, masses, BH spins, etc. The properties of the disk in the nonlinear regime, such as the persistence of nonaxisymmetric structures in realistic disk models, should also be addressed.

ACKNOWLEDGMENTS

The authors thank our colleagues Eloisa Bentivegna, Peter Diener, Juhan Frank, Tyler Landis, Frank Löffler, Luis Lehner, Christian D. Ott, Jorge Pullin, Jian Tao, Manuel Tiglio, and Joel Tohline for valuable discussions and ideas. We also thank Yasufumi Kojima for providing his data for comparison with our results (Fig. 11). This work is supported by NSF Grants No. 0721915 (Alpaca), No. 0904015 (CIGR), and No. 0905046/0941653 (PetaCactus). The simulations were performed using the supercomputing resources Ranger and Lonestar at TACC via the NSF TeraGrid and Queenbee at LONI. We also used the PetaShare infrastructure to store the data from our simulations. N. S. acknowledges the hospitality of the University of Tübingen, and O. K. acknowledges the hospitality of AEI numerical relativity group.

APPENDIX

1. Transforming initial data to horizon-penetrating coordinates

Here we present the transformation of the stationary axisymmetric initial data in quasi-isotropic coordinates to time-independent horizon-penetrating coordinates which is used in Sec. III in order to remove the degeneracy at the BH horizon. In our initial data, the metric is given in general form (6) and represents an axisymmetric deformation of a Schwarzschild BH by a massive equilibrium torus. The sought transformation has to satisfy the following requirements:

(i) The metric in the new coordinates is time-independent;
(ii) the metric does not have pathologies (degeneracy or divergence) at the event horizon;
(iii) the three-metric on $t=$ const foliation is positive definite (i.e. the $t=$ const foliation is spacelike).

We build our transformation by analogy with the transformation from isotropic Boyer-Lindquist coordinates [170] to horizon-penetrating Kerr-Schild coordinates [171] of Schwarzschild spacetime (see also [172] for a general case of a rotating BH). In this case, the line element has the following form:

$$ds^2_{\mathrm{is}} = -\left(\frac{1-m/2r_*}{1+m/2r_*}\right)^2 dt^2 + \psi^4(dr_*^2 + r_*^2 d\Omega^2),$$

where m is the BH mass, r_* is the isotropic radius, $d\Omega^2 \equiv d\theta^2 + \sin\theta^2 d\varphi^2$ is the solid angle element, and $\psi \equiv 1 + \frac{m}{2r_*}$ is the conformal factor. At the event horizon $r_{*,h} = m/2$ the determinant of the isotropic metric is zero.

In the horizon-penetrating Kerr-Schild coordinates, the line element will be

$$ds^2_{\mathrm{ks}} = -(1-H)d\bar{t}^2 + 2Hd\bar{t}dr + (1+H)dr^2 + r^2 d\Omega^2,$$

where $H \equiv 2m/r$ and $r \equiv r_*(1 + m/2r_*)^2$ is the Schwarzschild radial coordinate.

The Jacobian of the transformation from the isotropic $(t, r_*, \theta, \varphi)$ to the horizon-penetrating coordinates $(\bar{t}, r, \theta, \varphi)$ has the following form:

$$\frac{D(t, r_*, \theta, \varphi)}{D(\bar{t}, r, \theta, \varphi)} = \begin{bmatrix} 1 & -\frac{H}{1-H} & 0 & 0 \\ 0 & \frac{r_*}{r\sqrt{1-H}} & 0 & 0 \\ 0 & 0 & 1 & 0 \\ 0 & 0 & 0 & 1 \end{bmatrix}.$$

The metric in the new coordinates remains independent of time, which is also true for an arbitrary transformation with the following Jacobian:

$$\frac{D(t, r_*, \theta, \varphi)}{D(\bar{t}, r, \theta, \varphi)} = \begin{bmatrix} 1 & f(r,\theta) & h(r,\theta) & 0 \\ 0 & g(r,\theta) & p(r,\theta) & 0 \\ 0 & 0 & 1 & 0 \\ 0 & 0 & 0 & 1 \end{bmatrix}, \qquad \text{(A1)}$$

where the functions $\{f, g, h, p\}$ do not explicitly depend on time and are only constrained by the regular Jacobian integrability conditions:

$$\frac{\partial f(r,\theta)}{\partial\theta} = \frac{\partial h(r,\theta)}{\partial r}, \qquad \frac{\partial g(r,\theta)}{\partial\theta} = \frac{\partial p(r,\theta)}{\partial r}.$$

For the case of a general axisymmetric spacetime, the metric in quasi-isotropic coordinates is given by

$$\mathbf{g}_{\mathbf{is}} \equiv \begin{bmatrix} g_{tt} & 0 & 0 & -\omega g_{\varphi\varphi} \\ 0 & e^{2\alpha} & 0 & 0 \\ 0 & 0 & r^2 e^{2\alpha} & 0 \\ -\omega g_{\varphi\varphi} & 0 & & g_{\varphi\varphi} \end{bmatrix},$$

where $g_{tt} \equiv -\lambda^2 + \omega^2 g_{\varphi\varphi}$ and $g_{\varphi\varphi} \equiv B^2\lambda^{-2}r_*^2\sin\theta^2$. We can select the set of functions $\{f, g, h, p\}$ in the Jacobian (A1) above to construct a transformation from the quasi-isotropic to horizon-penetrating coordinates, which satisfies the above requirements for an arbitrary stationary axisymmetric deformation of Schwarzschild if we choose

$$f(r,\theta) = 1 - 1/\lambda^2(r,\theta), \quad g(r,\theta) = e^{-\alpha(r,\theta)}/\lambda(r,\theta).$$

Since the metric potentials $\lambda(r_*, \theta)$ and $\alpha(r_*, \theta)$ are known as functions of r_* and not r, we need to express the new radial coordinate r in terms of r_*. The required relations in the following differential form are obtained by inverting the Jacobian (A1):

$$\left(\frac{\partial r_*}{\partial r}\right)_{\theta=\mathrm{const}} = \frac{1}{g(r_*,\theta)}, \qquad \left(\frac{\partial r_*}{\partial\theta}\right)_{r_*=\mathrm{const}} = 0.$$

These need to be integrated along the radial coordinate from $r_{*,h}$ to r_* for each θ:

$$r(r_*,\theta) - r_h = \int_{r_{*,h}}^{r_*} \frac{d\zeta}{g(\zeta,\theta)} = \int_{r_{*,h}}^{r_*} \lambda(\zeta,\theta)e^{\alpha(\zeta,\theta)}d\zeta,$$

where r_h is the radius of the event horizon in new coordinates. The remaining two unknown functions h and p can be calculated by 1D integration of the Jacobian integrability conditions:

$$h(r,\theta) = \int_{r_h}^{r} dr' \frac{\partial f(r',\theta)}{\partial\theta} = 2\int_{r_{*,h}}^{r_*} \frac{\lambda'_\theta(\zeta,\theta)e^{\alpha(\zeta,\theta)}}{\lambda^2(\zeta,\theta)}d\zeta,$$

$$p(r,\theta) = \int_{r_h}^{r} dr' \frac{\partial g(r',\theta)}{\partial\theta}$$

$$= -\int_{r_{*,h}}^{r_*}\left(\alpha'_\theta(\zeta,\theta) + \frac{\lambda'_\theta(\zeta,\theta)}{\lambda(\zeta,\theta)}\right)d\zeta.$$

After the transformation, the metric in the new horizon-penetrating coordinates has the following form:

TABLE VII. Physical parameters of the uniformly rotating polytropic star used for the code tests, in geometrized and CGS units, where R_p/R_e is the ratio of the polar to equatorial radii of the star, J/M^2 is its angular momentum, normalized with the square of the ADM mass of the star M, and $T/|W|$ is the ratio of the kinetic to binding energy of the star.

	Geom.	CGS
Polytropic scale K	100	1.46×10^5 cm^5 g^{-1} s^{-2}
Polytropic index Γ	2	2
Central rest-mass density ρ_c	0.001	6.17×10^{14} g cm^{-3}
Ratio R_p/R_e	0.7	0.7
ADM mass M	1.49	1.49
Rest mass M_0	1.59	1.59
Equatorial radius R_e	12.32	1.823×10^6 cm
Angular momentum J	1.32	1.16×10^{49} g cm^2 s^{-2}
Normalized ang. mom. J/M^2	0.59	0.59
Kinetic/binding en. $T/|W|$	0.0748	0.0748
Angular velocity Ω	0.0215	4300 s^{-1}
Keplerian angular velocity Ω_K	0.0286	5801 s^{-1}
Rotational period P	292.1	1.44×10^{-3} s

$$\mathbf{g_{ks}} \equiv \begin{bmatrix} g_{tt} & f g_{tt} & h g_{tt} & -\omega g_{\varphi\varphi} \\ \dots & e^{2\alpha} g^2 + g_{tt} f^2 & f h g_{tt} + e^{2\alpha} g p & -\omega f g_{\varphi\varphi} \\ \dots & \dots & h^2 g_{tt} + e^{2\alpha}(p^2 + r_*^2) & -\omega h g_{\varphi\varphi} \\ \dots & \dots & \dots & g_{\varphi\varphi} \end{bmatrix},$$

where ellipsis indicate matrix elements which can be filled in by symmetry. In the limit of $r \to r_h$, the functions f and g tend to infinity, while h and p vanish. The resulting metric at the horizon remains finite and nondegenerate:

$$\lim_{r\to r_h} \mathbf{g_{ks}} \equiv \begin{bmatrix} 0 & 1 & 0 & 0 \\ 1 & 2 & C & 0 \\ 0 & C & e^{2\alpha} r_*^2 & 0 \\ 0 & 0 & 0 & g_{\varphi\varphi} \end{bmatrix},$$

where $C \equiv \lim_{r\to r_h}[f h g_{tt} + e^{2\alpha} g p]$ is a finite constant.

2. Stable evolution of a uniformly rotating polytrope

In this section, we present results of testing the time evolution of a uniformly rotating polytropic star for numerical stability and convergence. In our tests, we use geometrized units based on the solar mass, in which $G = c = \mathcal{M}_\odot = 1$. The parameters of the star in the geometrized and CGS units are summarized in Table VII. We use a 13-block cubed sphere system that was described in [102] [see Fig. 1(b) and the related discussion in Sec. II A above]. For the current setup, we fix the sizes of the blocks by choosing $r_0 = 2.5$, $r_1 = 9$, and $r_2 = 14$ (see Sec. 4 of [102] for the definition of r_0, r_1, and r_2), with each block having an equal number of N^3 grid cells. The sizes of the domain and its blocks are selected in such a way that the star occupies $\approx 90\%$ of the entire domain in the radial equatorial direction, and the inner seven blocks of the system lie inside the star. This setup allows one to test how much the accuracy and convergence of our numerical scheme are affected by interpolation errors on the interblock boundaries which thread the bulk of the star.

The stability of the numerical scheme for evolving the spacetime metric depends on the numerical dissipation parameter ϵ [144] and the constraint damping coefficients κ and γ_2 (see Sec. II E). In general, higher values of numerical dissipation restrict the time step, while lower values are undesirable because they do not provide enough suppression of the numerical noise, which needs to be dissipated for stability [173]. For the current setup, we choose $\epsilon = 0.2$ and $\kappa = \gamma_2 = 0.1$. Values of the constraint damping parameters higher than ≈ 0.5 lead to numerical instabilities in our simulations of stars.

Initial data for the time evolution are generated by the RNS code [150], which uses the Komatsu-Eriguchi-Hachisu (Stergioulas-Friedman) method [150,152] to produce equilibrium models of stationary rotating relativistic stars. Since RNS is a 2D solver which uses its own grid that is different from the 3D multiblock grid of our time-evolution code, we interpolate the data from the 2D grid to the 3D multiblock grid using fourth-order Lagrange interpolation. Also, because the variables in the generalized harmonic formulation contain first derivatives of the metric and because the resolution on the 2D grid is usually much higher than on the multiblock 3D grid, we perform numerical differentiation on the 2D grid. The resulting derivatives are then interpolated onto the 3D grid. Note that the interpolation procedure is not consistent with the Einstein constraint equations and hence produces numerical noise.

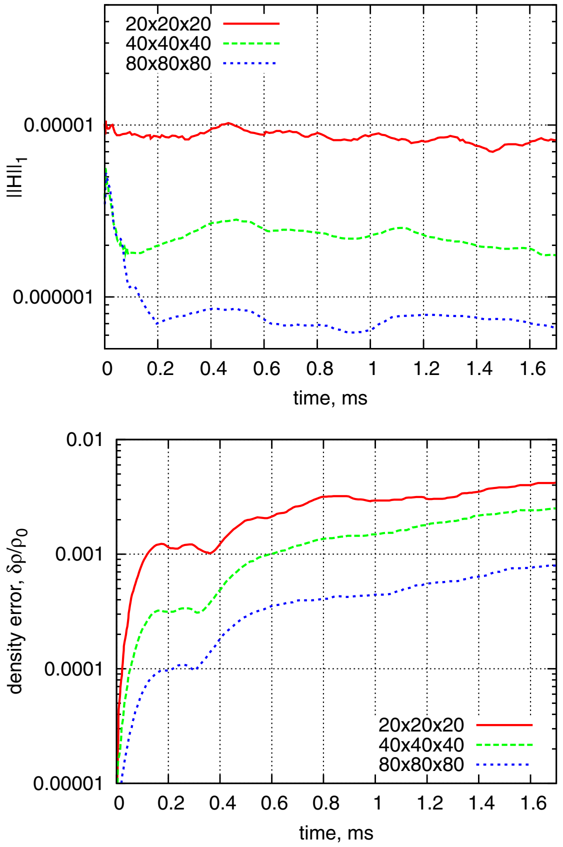

FIG. 18 (color online). Time evolution of L_1 norms of the Hamiltonian constraint (top) and density solution error $\delta\rho/\rho_{\max}(0)$ (bottom) for three different resolutions.

The system is evolved up to $t = 350$, which corresponds to 1.73 ms or 10 dynamical time scales of the star.[10] In vacuum regions outside the star, we use an artificial atmosphere, which has a density of $\rho_{\mathrm{atm}} = 10^{-7}\rho_{\max}(0)$, where $\rho_{\max}(0)$ is the maximum density at $t = 0$. If during the evolution the density in a cell drops down below a threshold value set to $\rho_{\mathrm{thr}} = 2\rho_{\mathrm{atm}}$, the density in this cell is reset to the artificial atmospheric value. To estimate the accuracy of our code, we have performed a convergence study using three different resolutions with $N^3 = 20 \times 20 \times 20$, $40 \times 40 \times 40$, and $80 \times 80 \times 80$ grid points in each block. We have analyzed various integral norms of the errors in all evolved variables, including 50 spacetime variables, 5 primitive variables, and 5 conserved variables. We have also analyzed integral norms of the Hamiltonian and momentum constraints, as well as the behavior of conserved integral quantities such as total rest mass and total angular momentum.

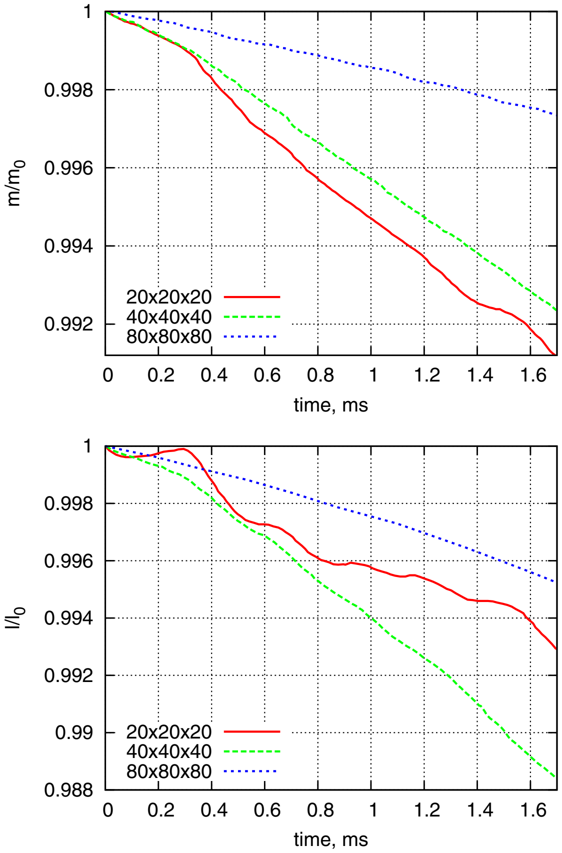

FIG. 19 (color online). Time evolution of the total rest mass (top) and the total angular momentum (bottom) for three different resolutions. Both quantities are normalized to their values at $t = 0$.

In all cases, we observe the expected second-order convergence. As an example, Fig. 18 (top panel) shows the time evolution of the L_1 norm of the normalized density deviation $\delta\rho \equiv [\rho(t) - \rho(0)]/\rho_{\max}(0)$ for the three resolutions. Because of accumulation of truncation errors, this deviation exhibits a steady growth (modulo small variations because of oscillations of the star) throughout the entire evolution. The deviation for $N = 40$ is larger than that for $N = 80$ by a factor of ≈ 4, which is a clear signature of second-order convergence. However, the deviation for $N = 20$ is larger than that for $N = 40$ by a smaller factor of ≈ 1.5, which means that the resolution $N = 20$ is insufficient for achieving a convergent regime. A similar convergent behavior is observed for integral norms of the deviations of all of the rest of the variables.

Figure 18 (bottom panel) shows the plot of the L_1 norm of the Hamiltonian constraint violation as a function of time. This quantity is not zero at $t = 0$, since initial conditions were interpolated from the 2D grid and interpolation errors were introduced. However, because of the constraint damping scheme, the Hamiltonian constraint violation significantly drops for medium and high resolutions within the first 0.2 ms. During subsequent evolution the value of the Hamiltonian constraint remains stable and clearly shows second-order convergence with resolution;

---

[10] The dynamical time t_D is defined as $t_D = R_e\sqrt{R_e/M}$, where R_e is a proper equatorial circumferential radius and M the Arnowitt-Deser-Misner (ADM) mass of the star. It corresponds to the inverse of the orbital frequency $\Omega = \sqrt{M/R_e^3}$ at R_e.

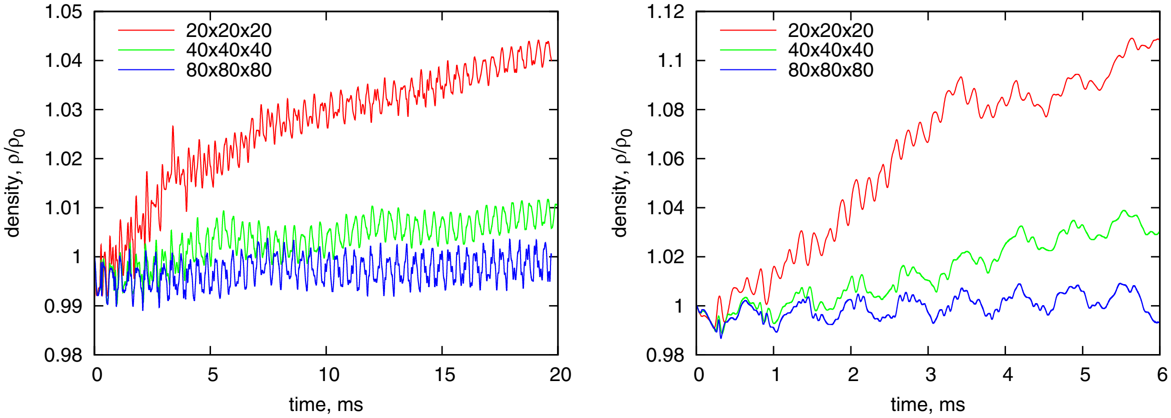

FIG. 20 (color online). Time evolution of the density $\rho_c(t)$ at the center of a TOV star, normalized by its initial value ρ_0, for three different resolutions. Left: The Cowling approximation. Right: The fully dynamical GR case.

i.e. the values of the Hamiltonian constraint for $N = 20$, 40, and 80 are in an approximate ratio 16:4:1. Momentum constraints show a similar behavior.

Figure 19 demonstrates time evolution of the total rest mass (upper panel) and total angular momentum (lower panel) of the star. In our numerical simulations these quantities are not conserved mostly due to interpolation errors on the interblock boundaries that pass through the bulk of the star. By the end of the simulation, for $N = 20$, 40, and 80, the total rest mass decreases by 0.88%, 0.84%, and 0.25%, respectively, while the total angular momentum decreases by 0.07%, 0.12%, and 0.05%, respectively. These numbers show that the smallest necessary resolution for the convergent regime is $N = 40$, which amounts to ≈ 70–100 points across the star.

3. Fundamental modes of a Tolman-Oppenheimer-Volkoff (TOV) star

As another test of the coupling between the GR and hydro parts of the code, we evolved a TOV solution on a seven-block system and measured the frequencies of its fundamental oscillations both in the Cowling approximation and in full GR. In these tests, we use geometrized units in which $G = c = \mathcal{M}_\odot = 1$. We choose a star with $\Gamma = 2$, $K = 100$, and the value of rest-mass density in the center $\rho_c = 1.28 \times 10^{-3}$. These parameters produce a TOV star with gravitational mass $M = 1.4$ and circumferential radius $R_e = 9.8$. This system has already been extensively studied in the literature and used for the assessment of relativistic hydrodynamical codes (e.g., [165,174]). The seven-block cubed sphere system that we used [see Fig. 1(a)] has the outer radius $R = 12$, which makes the star occupy 82% of the domain in the radial direction and leaves extra room for small oscillations. The size of the cubical block in the center is $a = 4.8$, placing it completely inside the star. The bulk of the star is therefore threaded by interpolation boundaries between the blocks. The cubical block contains N^3 volume cells, and the outer blocks have $N^2 \times (2N)$ cells. For the tests, we used resolutions $N = 20$, 40, and 80, which roughly correspond to 40, 80, and 160 points across the star.

To observe and measure the fundamental mode, we artificially add a small initial perturbation, roughly corresponding to the shape of the mode:

$$\frac{\delta\rho}{\rho} = A \cos\frac{\pi r}{2R_e}.$$

The amplitude was chosen to be $A = 0.005$. Figure 20 displays the resulting oscillatory behavior of the rest-mass density in the center of the star for three different resolutions. The left and right panels correspond to fixed (Cowling approximation) and dynamical spacetime geometries, respectively. Oscillations of the density are

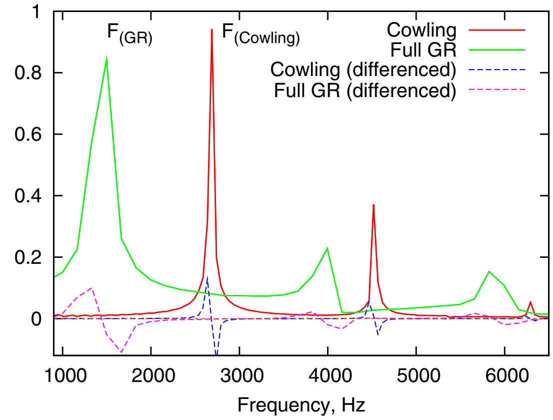

FIG. 21 (color online). Power spectrum of the density oscillations $\rho_c(t)$ at the center of a TOV star for the highest resolution simulations in the Cowling approximation (red solid line) and in full GR (green solid line). Also shown are derivatives of the power spectrum with respect to the frequency, obtained using the central finite-differencing scheme. The derivatives allow one to localize peaks in the power spectrum more accurately. The vertical axis has arbitrary units.

accompanied by a secular drift, which reflects accumulation of truncation errors and converges away with resolution at approximately second-order convergence rate. Conserved quantities such as the total rest mass and the total angular momentum (not shown) also exhibit the second-order convergence, as expected. In particular, for the Cowling approximation case, the simulation continued up to 20 ms, and the final rest mass is conserved up to 8.3%, 3.7%, and 1.1% for resolutions with $N = 20$, 40, and 80, respectively. For the full GR case, the simulation continued for 6 ms and the rest mass is conserved up to 3.2%, 1.3%, and 0.4%, respectively, for the same three resolutions. This shows that the rate of the mass loss in the Cowling and full GR simulations is approximately the same, as expected. Because the bulk of the star is threaded by interpolation boundaries between the blocks, the mass loss is significantly higher in this setup than in the case of a regular Cartesian grid, where we normally observe that the mass is conserved up to 7–8 significant digits for a similar resolution.

A Fourier transform of $\rho_c(t)$ allows one to measure the frequencies of the dominant oscillation modes. Figure 21 shows the Fourier power spectrum of $\rho_c(t)$ in the Cowling and full GR cases for simulations with the highest resolution $N = 80$. Both spectra contain three easily identifiable peaks corresponding to the fundamental radial modes F, H_1, and H_2. The same plot also shows derivatives of the spectral power with respect to the frequency, computed using the central finite-differencing scheme. Zeros of these numerical derivatives provide accurate estimates of the location of frequency peaks. The frequency of the F mode in the Cowling approximation is $\nu(F) = 2.684(40)$ kHz, which is in agreement with the value of 2.706 kHz, found in [165]. In the fully general-relativistic case, we obtain the frequency $\nu(F) = 1.440(50)$ kHz, which also agrees with the value 1.458 kHz, found in [164]. Note that the error in the values of fundamental frequencies above is estimated as the distance between the root of the power spectrum derivative and the nearest point with a nonzero value.

---

[1] S. E. Woosley, Astrophys. J. **405**, 273 (1993).

[2] S. E. Woosley and J. S. Bloom, Annu. Rev. Astron. Astrophys. **44**, 507 (2006).

[3] Y. Sekiguchi and M. Shibata, arXiv:1009.5303.

[4] D. Proga, A. I. MacFadyen, P. J. Armitage, and M. C. Begelman, Astrophys. J. **599**, L5 (2003).

[5] S. Fujimoto, K. Kotake, S. Yamada, M. Hashimoto, and K. Sato, Astrophys. J. **644**, 1040 (2006).

[6] L. Dessart, A. Burrows, E. Livne, and C. D. Ott, Astrophys. J. **673**, L43 (2008).

[7] E. O'Connor and C. D. Ott, arXiv:1010.5550.

[8] S. Nagataki, Astrophys. J. **704**, 937 (2009).

[9] S. Harikae, T. Takiwaki, and K. Kotake, Astrophys. J. **704**, 354 (2009).

[10] D. Lopez-Camara, W. H. Lee, and E. Ramirez-Ruiz, Astrophys. J. **692**, 804 (2009).

[11] A. I. MacFadyen and S. E. Woosley, Astrophys. J. **524**, 262 (1999).

[12] A. I. MacFadyen, S. E. Woosley, and A. Heger, Astrophys. J. **550**, 410 (2001).

[13] M. Shibata and K. Taniguchi, Phys. Rev. D **73**, 064027 (2006).

[14] L. Baiotti, B. Giacomazzo, and L. Rezzolla, Phys. Rev. D **78**, 084033 (2008).

[15] L. Baiotti, B. Giacomazzo, and L. Rezzolla, Classical Quantum Gravity **26**, 114005 (2009).

[16] Y. T. Liu, S. L. Shapiro, Z. B. Etienne, and K. Taniguchi, Phys. Rev. D **78**, 024012 (2008).

[17] B. Giacomazzo, L. Rezzolla, and L. Baiotti, Mon. Not. R. Astron. Soc. **399**, L164 (2009).

[18] K. Kiuchi, Y. Sekiguchi, M. Shibata, and K. Taniguchi, Phys. Rev. D **80**, 064037 (2009).

[19] M. D. Duez, Classical Quantum Gravity **27**, 114002 (2010).

[20] L. Rezzolla, L. Baiotti, B. Giacomazzo, D. Link, and J. A. Font, Classical Quantum Gravity **27**, 114105 (2010).

[21] M. Ruffert, M. Rampp, and H.-T. Janka, Astron. Astrophys. **321**, 991 (1997).

[22] M. Ruffert, H.-T. Janka, and G. Schäfer, Astron. Astrophys. **311**, 532 (1996).

[23] M. Ruffert, H.-T. Janka, K. Takahashi, and G. Schaefer, Astron. Astrophys. **319**, 122 (1997).

[24] M. Ruffert and H.-T. Janka, Astron. Astrophys. **338**, 535 (1998).

[25] R. Oechslin and H. Janka, Mon. Not. R. Astron. Soc. **368**, 1489 (2006).

[26] M. Anderson, E. W. Hirschmann, L. Lehner, S. L. Liebling, P. M. Motl, D. Neilsen, C. Palenzuela, and J. E. Tohline, Phys. Rev. D **77**, 024006 (2008).

[27] M. Anderson, E. W. Hirschmann, L. Lehner, S. L. Liebling, P. M. Motl, D. Neilsen, C. Palenzuela, and J. E. Tohline, Phys. Rev. Lett. **100**, 191101 (2008).

[28] S. Chawla, M. Anderson, M. Besselman, L. Lehner, S. L. Liebling, P. M. Motl, and D. Neilsen, Phys. Rev. Lett. **105**, 111101 (2010).

[29] M. Ruffert and H. Janka, Astron. Astrophys. **514**, A66 (2010).

[30] M. Shibata and K. Uryū, Phys. Rev. D **74**, 121503 (2006).

[31] M. Shibata and K. Uryu, Classical Quantum Gravity **24**, S125 (2007).

[32] F. Foucart, M. D. Duez, L. E. Kidder, and S. A. Teukolsky, Phys. Rev. D **83**, 024005 (2011).

[33] M. Shibata, K. Kyutoku, T. Yamamoto, and K. Taniguchi, Phys. Rev. D **79**, 044030 (2009).

[34] T. Yamamoto, M. Shibata, and K. Taniguchi, Phys. Rev. D **78**, 064054 (2008).
[35] Z. B. Etienne, Y. T. Liu, S. L. Shapiro, and T. W. Baumgarte, Phys. Rev. D **79**, 044024 (2009).
[36] M. D. Duez, F. Foucart, L. E. Kidder, C. D. Ott, and S. A. Teukolsky, Classical Quantum Gravity **27**, 114106 (2010).
[37] E. Rantsiou, S. Kobayashi, P. Laguna, and F. A. Rasio, Astrophys. J. **680**, 1326 (2008).
[38] R. Popham, S. E. Woosley, and C. Fryer, Astrophys. J. **518**, 356 (1999).
[39] T. Piran, Rev. Mod. Phys. **76**, 1143 (2005).
[40] W. H. Lee and E. Ramirez-Ruiz, New J. Phys. **9**, 17 (2007).
[41] P. Meszaros and M. J. Rees, Mon. Not. R. Astron. Soc. **257**, 29P (1992).
[42] N. Gehrels, E. Ramirez-Ruiz, and D. B. Fox, Annu. Rev. Astron. Astrophys. **47**, 567 (2009).
[43] R. D. Blandford and R. L. Znajek, Mon. Not. R. Astron. Soc. **179**, 433 (1977).
[44] V. V. Usov, Nature (London) **357**, 472 (1992).
[45] B. D. Metzger, arXiv:1001.5046.
[46] J. Frank, A. King, and D. J. Raine, *Accretion Power in Astrophysics* (Cambridge University Press, Cambridge, England, 2002), 3rd ed.
[47] S. Rosswog and M. B. Davies, Mon. Not. R. Astron. Soc. **334**, 481 (2002).
[48] M. Lyutikov, arXiv:0911.0349.
[49] S. E. Woosley, A. Heger, and T. A. Weaver, Rev. Mod. Phys. **74**, 1015 (2002).
[50] Y. Sekiguchi and M. Shibata, Prog. Theor. Phys. **117**, 1029 (2007).
[51] L. Dessart, C. D. Ott, A. Burrows, S. Rosswog, and E. Livne, Astrophys. J. **690**, 1681 (2009).
[52] S. Rosswog and M. Liebendörfer, Mon. Not. R. Astron. Soc. **342**, 673 (2003).
[53] M. J. Rees and P. Meszaros, Mon. Not. R. Astron. Soc. **258**, 41P (1992).
[54] J. Goodman, A. Dar, and S. Nussinov, Astrophys. J. **314**, L7 (1987).
[55] M. Jaroszynski, Acta Astronomica **43**, 183 (1993).
[56] P. Mészáros, Rep. Prog. Phys. **69**, 2259 (2006).
[57] S. Kobayashi, B. Zhang, P. Mészáros, and D. Burrows, Astrophys. J. **655**, 391 (2007).
[58] E. Nakar and T. Piran, Astrophys. J. **598**, 400 (2003).
[59] B. Zhang, Y. Z. Fan, J. Dyks, S. Kobayashi, P. Mészáros, D. N. Burrows, J. A. Nousek, and N. Gehrels, Astrophys. J. **642**, 354 (2006).
[60] M. A. Abramowicz, M. Calvani, and L. Nobili, Nature (London) **302**, 597 (1983).
[61] J. C. B. Papaloizou and J. E. Pringle, Mon. Not. R. Astron. Soc. **208**, 721 (1984).
[62] J. C. B. Papaloizou and J. E. Pringle, Mon. Not. R. Astron. Soc. **213**, 799 (1985).
[63] Y. Kojima, Prog. Theor. Phys. **75**, 251 (1986).
[64] J. W. Woodward, J. E. Tohline, and I. Hachisu, Astrophys. J. **420**, 247 (1994).
[65] J. A. Font and F. Daigne, Mon. Not. R. Astron. Soc. **334**, 383 (2002).
[66] O. Zanotti, L. Rezzolla, and J. A. Font, Mon. Not. R. Astron. Soc. **341**, 832 (2003).
[67] B. Paczynsky and P. J. Wiita, Astron. Astrophys. **88**, 23 (1980).
[68] D. B. Wilson, Nature (London) **312**, 620 (1984).
[69] M. A. Abramowicz, V. Karas, and A. Lanza, Astron. Astrophys. **331**, 1143 (1998).
[70] F. Daigne and R. Mochkovitch, Mon. Not. R. Astron. Soc. **285**, L15 (1997).
[71] J. A. Font and F. Daigne, Astrophys. J. **581**, L23 (2002).
[72] F. Daigne and J. A. Font, Mon. Not. R. Astron. Soc. **349**, 841 (2004).
[73] R. Khanna and S. K. Chakrabarti, Mon. Not. R. Astron. Soc. **259**, 1 (1992).
[74] N. Masuda, S. Nishida, and Y. Eriguchi, Mon. Not. R. Astron. Soc. **297**, 1139 (1998).
[75] S. Nishida, A. Lanza, Y. Eriguchi, and M. A. Abramowicz, Mon. Not. R. Astron. Soc. **278**, L41 (1996).
[76] P. J. Montero, J. A. Font, and M. Shibata, Phys. Rev. Lett. **104**, 191101 (2010).
[77] V. S. Safronov, Ann. Astrophys. **23**, 979 (1960).
[78] A. Toomre, Astrophys. J. **139**, 1217 (1964).
[79] C. F. Gammie, Astrophys. J. **553**, 174 (2001).
[80] Y. Kojima, Prog. Theor. Phys. **75**, 1464 (1986).
[81] M. Abramowicz, M. Jaroszynski, and M. Sikora, Astron. Astrophys. **63**, 221 (1978).
[82] P. Goldreich, J. Goodman, and R. Narayan, Mon. Not. R. Astron. Soc. **221**, 339 (1986).
[83] O. M. Blaes and W. Glatzel, Mon. Not. R. Astron. Soc. **220**, 253 (1986).
[84] R. Narayan, P. Goldreich, and J. Goodman, Mon. Not. R. Astron. Soc. **228**, 1 (1987).
[85] J. Frank and J. A. Robertson, Mon. Not. R. Astron. Soc. **232**, 1 (1988).
[86] W. H. Zurek and W. Benz, Astrophys. J. **308**, 123 (1986).
[87] O. M. Blaes, Mon. Not. R. Astron. Soc. **227**, 975 (1987).
[88] O. M. Blaes and J. F. Hawley, Astrophys. J. **326**, 277 (1988).
[89] J. Goodman and R. Narayan, Mon. Not. R. Astron. Soc. **231**, 97 (1988).
[90] D. M. Christodoulou and R. Narayan, Astrophys. J. **388**, 451 (1992).
[91] D. M. Christodoulou, Astrophys. J. **412**, 696 (1993).
[92] F. C. Adams, S. P. Ruden, and F. H. Shu, Astrophys. J. **347**, 959 (1989).
[93] F. H. Shu, S. Tremaine, F. C. Adams, and S. P. Ruden, Astrophys. J. **358**, 495 (1990).
[94] M. H. M. Heemskerk, J. C. Papaloizou, and G. J. Savonije, Astron. Astrophys. **260**, 161 (1992).
[95] P. A. Taylor, J. C. Miller, and P. Podsiadlowski, arXiv:1006.4624 [Mon. Not. R. Astron. Soc. (to be published)].
[96] M. H. P. M. van Putten, Phys. Rev. Lett. **87**, 091101 (2001).
[97] T. Goodale, G. Allen, G. Lanfermann, J. Massó, T. Radke, E. Seidel, and J. Shalf, in *Vector and Parallel Processing—VECPAR'2002, 5th International Conference*, Lect. Notes Comput. Sci. (Springer, Berlin, 2003).
[98] Cactus Web site, http://www.cactuscode.org.
[99] E. Schnetter, S. H. Hawley, and I. Hawke, Classical Quantum Gravity **21**, 1465 (2004).
[100] Carpet Web site, http://www.carpetcode.org/.

[101] E. Schnetter, P. Diener, E. N. Dorband, and M. Tiglio, Classical Quantum Gravity **23**, S553 (2006).
[102] B. Zink, E. Schnetter, and M. Tiglio, Phys. Rev. D **77**, 103015 (2008).
[103] E. Pazos, E. N. Dorband, A. Nagar, C. Palenzuela, E. Schnetter, and M. Tiglio, Classical Quantum Gravity **24**, S341 (2007).
[104] L. Lindblom, M. A. Scheel, L. E. Kidder, R. Owen, and O. Rinne, Classical Quantum Gravity **23**, S447 (2006).
[105] J. Thornburg, Classical Quantum Gravity **4**, 1119 (1987).
[106] J. Thornburg, Ph.D. thesis, University of British Columbia, Vancouver, British Columbia, 1993.
[107] R. Gómez, L. Lehner, R. L. Marsa, and J. Winicour, Phys. Rev. D **57**, 4778 (1998).
[108] R. Gómez, R. L. Marsa, and J. Winicour, Phys. Rev. D **56**, 6310 (1997).
[109] R. Gómez *et al.*, Phys. Rev. Lett. **80**, 3915 (1998).
[110] S. Bonazzola, E. Gourgoulhon, and J.-A. Marck, arXiv:gr-qc/9904040.
[111] L. E. Kidder, M. A. Scheel, and S. A. Teukolsky, Phys. Rev. D **64**, 064017 (2001).
[112] E. Gourgoulhon, P. Grandclément, K. Taniguchi, J. A. Marck, and S. Bonazzola, Phys. Rev. D **63**, 064029 (2001).
[113] P. Grandclément, S. Bonazzola, E. Gourgoulhon, and J.-A. Marck, J. Comput. Phys. **170**, 231 (2001).
[114] H. P. Pfeiffer, L. E. Kidder, M. A. Scheel, and S. A. Teukolsky, Comput. Phys. Commun. **152**, 253 (2003).
[115] J. Thornburg, Classical Quantum Gravity **21**, 3665 (2004).
[116] G. Calabrese and D. Neilsen, Phys. Rev. D **71**, 124027 (2005).
[117] M. A. Scheel, H. P. Pfeiffer, L. Lindblom, L. E. Kidder, O. Rinne, and S. A. Teukolsky, Phys. Rev. D **74**, 104006 (2006).
[118] H. P. Pfeiffer, D. Brown, L. E. Kidder, L. Lindblom, G. Lovelance, and M. A. Scheel, Classical Quantum Gravity **24**, S59 (2007).
[119] F. Foucart, L. E. Kidder, H. P. Pfeiffer, and S. A. Teukolsky, Phys. Rev. D **77**, 124051 (2008).
[120] M. D. Duez, F. Foucart, L. E. Kidder, H. P. Pfeiffer, M. A. Scheel, and S. A. Teukolsky, Phys. Rev. D **78**, 104015 (2008).
[121] E. Pazos, M. Tiglio, M. D. Duez, L. E. Kidder, and S. A. Teukolsky, Phys. Rev. D **80**, 024027 (2009).
[122] P. C. Fragile, C. C. Lindner, P. Anninos, and J. D. Salmonson, Astrophys. J. **691**, 482 (2009).
[123] M. A. Scheel, M. Boyle, T. Chu, L. E. Kidder, K. D. Matthews, and H. P. Pfeiffer, Phys. Rev. D **79**, 024003 (2009).
[124] C. Ronchi, J. Comput. Phys. **124**, 93 (1996).
[125] G. Calabrese and D. Neilsen, Phys. Rev. D **69**, 044020 (2004).
[126] B. Szilágyi, D. Pollney, L. Rezzolla, J. Thornburg, and J. Winicour, Classical Quantum Gravity **24**, S275 (2007).
[127] C. Reisswig, N. T. Bishop, D. Pollney, and B. Szilágyi, Classical Quantum Gravity **27**, 075014 (2010).
[128] L. D. Landau and E. M. Lifshitz, *The Classical Theory of Fields, Course of Theoretical Physics* (Elsevier Butterworth-Heinemann, Oxford, 2004), Vol. 2.
[129] J. R. Wilson, Astrophys. J. **173**, 431 (1972).
[130] J. A. Font, Living Rev. Relativity **6**, 4 (2003), http://www.livingreviews.org/lrr-2008-7.
[131] F. Banyuls, J. A. Font, J. M. Ibáñez, J. M. Martí, and J. A. Miralles, Astrophys. J. **476**, 221 (1997).
[132] C. F. Gammie, J. C. McKinney, and G. Tóth, Astrophys. J. **589**, 444 (2003).
[133] P. Colella and P. Woodward, J. Comput. Phys. **54**, 174 (1984).
[134] J. Martí and E. Müller, J. Comput. Phys. **123**, 1 (1996).
[135] A. Harten, P. Lax, and B. van Leer, SIAM Rev. **25**, 35 (1983).
[136] S. C. Noble, C. F. Gammie, J. C. McKinney, and L. Del Zanna, Astrophys. J. **641**, 626 (2006).
[137] L. Lindblom and B. Szilágyi, Phys. Rev. D **80**, 084019 (2009).
[138] P. Secchi, Diff. Integral Equ. **9**, 671 (1996).
[139] P. Secchi, Arch. Ration. Mech. Anal. **134**, 155 (1996).
[140] J. Rauch, Trans. Am. Math. Soc. **291**, 167 (1985).
[141] T. P. Liu, J. Diff. Equ. **33**, 92 (1979).
[142] B. Gustafsson, H.-O. Kreiss, and J. Oliger, *Time Dependent Problems and Difference Methods* (Wiley, New York, 1995).
[143] L. Lehner, O. Reula, and M. Tiglio, Classical Quantum Gravity **22**, 5283 (2005).
[144] P. Diener, E. N. Dorband, E. Schnetter, and M. Tiglio, J. Sci. Comput. **32**, 109 (2007).
[145] D. W. Neilsen and M. W. Choptuik, Classical Quantum Gravity **17**, 733 (2000).
[146] J. A. Font, H. Dimmelmeier, A. Gupta, and N. Stergioulas, Mon. Not. R. Astron. Soc. **325**, 1463 (2001).
[147] P. J. Montero, J. A. Font, and M. Shibata, Phys. Rev. D **78**, 064037 (2008).
[148] O. Korobkin, B. Aksoylu, M. Holst, E. Pazos, and M. Tiglio, Classical Quantum Gravity **26**, 145007 (2009).
[149] B. Zink, O. Korobkin, E. Schnetter, and N. Stergioulas, Phys. Rev. D **81**, 084055 (2010).
[150] N. Stergioulas and J. L. Friedman, Astrophys. J. **444**, 306 (1995).
[151] S. Nishida and Y. Eriguchi, Astrophys. J. **427**, 429 (1994).
[152] H. Komatsu, Y. Eriguchi, and I. Hachisu, Mon. Not. R. Astron. Soc. **237**, 355 (1989).
[153] M. Shibata, Phys. Rev. D **76**, 064035 (2007).
[154] J. D. Brown, Phys. Rev. D **77**, 044018 (2008).
[155] S. W. Andalib, J. E. Tohline, and D. M. Christodoulou, Astrophys. J. Suppl. Ser. **108**, 471 (1997).
[156] D. Brown, P. Diener, O. Sarbach, E. Schnetter, and M. Tiglio, Phys. Rev. D **79**, 044023 (2009).
[157] H. A. Williams and J. E. Tohline, Astrophys. J. **315**, 594 (1987).
[158] J. A. Font and F. Daigne, Mon. Not. R. Astron. Soc. **334**, 383 (2002).
[159] C. W. Misner, K. S. Thorne, and J. A. Wheeler, *Gravitation* (Freeman, San Francisco, 1973).
[160] E. Schnetter, Classical Quantum Gravity **20**, 4719 (2003).
[161] E. F. Toro, *Riemann Solvers and Numerical Methods for Fluid Dynamics* (Springer-Verlag, Berlin, 1999).
[162] A. T. Okazaki, S. Kato, and J. Fukue, Publ. Astron. Soc. Jpn. **39**, 457 (1987).
[163] L. Rezzolla, S. Yoshida, and O. Zanotti, Mon. Not. R. Astron. Soc. **344**, 978 (2003).

[164] H. Dimmelmeier, N. Stergioulas, and J. A. Font, Mon. Not. R. Astron. Soc. **368**, 1609 (2006).

[165] J. A. Font, T. Goodale, S. Iyer, M. Miller, L. Rezzolla, E. Seidel, N. Stergioulas, W.-M. Suen, and M. Tobias, Phys. Rev. D **65**, 084024 (2002).

[166] L. Baiotti, I. Hawke, P. J. Montero, F. Löffler, L. Rezzolla, N. Stergioulas, J. A. Font, and E. Seidel, Phys. Rev. D **71**, 024035 (2005).

[167] E. B. Abdikamalov, H. Dimmelmeier, L. Rezzolla, and J. C. Miller, Mon. Not. R. Astron. Soc. **392**, 52 (2009).

[168] C. D. Ott, Classical Quantum Gravity **26**, 063001 (2009).

[169] E. B. Abdikamalov, C. D. Ott, L. Rezzolla, L. Dessart, H. Dimmelmeier, A. Marek, and H. T. Janka, Phys. Rev. D **81**, 044012 (2010).

[170] S. R. Brandt and E. Seidel, Phys. Rev. D **54**, 1403 (1996).

[171] R. P. Kerr and A. Schild, Gen. Relativ. Gravit. **41**, 2485 (2009).

[172] R. Takahashi, Mon. Not. R. Astron. Soc. **382**, 567 (2007).

[173] G. Calabrese, L. Lehner, O. Reula, O. Sarbach, and M. Tiglio, Classical Quantum Gravity **21**, 5735 (2004).

[174] J. A. Font, N. Stergioulas, and K. D. Kokkotas, Mon. Not. R. Astron. Soc. **313**, 678 (2000).